

Diercks, J. S., Georgi, M., Herranz, J., Diklič, N., Chauhan, P., Clark, A. H., ... Schmidt, T. J. (2022). CO₂ electroreduction on unsupported PdPt aerogels: effects of alloying and surface composition on product selectivity. *ACS Applied Energy Materials*, 5(7), 8460–8471. <https://doi.org/10.1021/acsaem.2c00987>

CO₂ electroreduction on unsupported PdPt aerogels: Effects of alloying and surface composition on product selectivity

Justus S. Diercks,[†] Maximilian Georgi,[‡] Juan Herranz,^{†,} Nataša Diklic,[†] Piyush Chauhan,[†] Adam H. Clark,[§] René Hübner,[◇] Antoine Faisnel,[†] Qin hao Chen,[†] Maarten Nachtegaal,[§] Alexander Eychmüller,[‡] and Thomas J. Schmidt^{†,‡}*

[†] Electrochemistry Laboratory, Paul Scherrer Institut, 5232 Villigen-PSI, Switzerland

[‡] Physical Chemistry, Technical University Dresden, 01062 Dresden, Germany

[§] Laboratory for Synchrotron Radiation and Femtochemistry, Paul Scherrer Institute, 5232 Villigen-PSI, Switzerland

[◇] Institute of Ion Beam Physics and Materials Research, Helmholtz-Zentrum Dresden-Rossendorf, 01328 Dresden, Germany

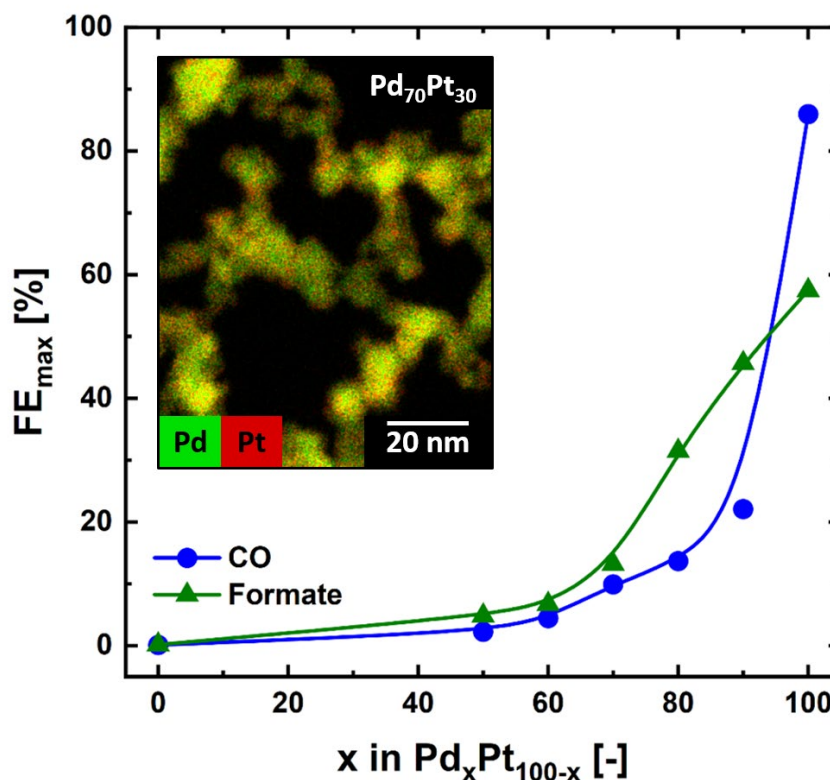
[‡] Laboratory of Physical Chemistry, ETH Zurich, 8093 Zurich, Switzerland

KEYWORDS

CO₂ electroreduction, selectivity, bimetallic aerogel, PdPt alloy, homogeneity

1 ABSTRACT

2 Due to its unique ability to reduce carbon dioxide (CO_2) into CO or formate at high vs. low overpotentials,
 3 respectively, palladium is a promising catalyst for the electrochemical CO_2 -reduction reaction (CO_2RR).
 4 Further improvements aim at increasing its activity and selectivity toward either of these value-added
 5 species while reducing the amount of hydrogen produced as a side-product. With this motivation, in this
 6 work, we synthesized a range of unsupported, bimetallic PdPt- as well as pure Pt- or Pd-aerogels and
 7 extensively characterized them using various microscopic and spectroscopic techniques. These revealed
 8 that the aerogels' porous web consists of homogenous alloys of Pt and Pd, with palladium and platinum
 9 being present on their surface for all compositions. The subsequent determination of these aerogels'
 10 CO_2RR -performance unveiled that the high activity of these Pt surface atoms toward hydrogen evolution
 11 causes all PdPt alloys to favor this reaction over CO_2 -reduction. In the case of the pure Pd aerogel, though,
 12 its unsupported nature leads to a suppression of H_2 -evolution and a concomitant increase in the selectivity
 13 toward CO when compared to a commercial, carbon-supported Pd-nanoparticle catalyst.



1. INTRODUCTION

The electrochemical conversion of carbon dioxide (CO₂) into value-added products in near-neutral aqueous electrolytes is the subject of continuous research interest, as it enables the use of CO₂ as a reactant whose emissions are increasingly taxed in many countries.¹ This interest is further driven by the possibility to electroreduce CO₂ into products of known value for the chemical industry, with electrochemical carbon monoxide (CO) or formate production having been hypothesized to be economically competitive with regard to industrial pathways.² In this context, palladium-based catalysts possess great intrinsic interest, since they have been repeatedly shown to display high selectivities for CO and formate at high vs. low overpotentials, respectively.³⁻⁵ Concomitantly, hydrogen (H₂) is electrochemically produced in significant amounts across the entire CO₂-reduction reaction (CO₂RR) potential range. This side reaction becomes particularly problematic for carbon-supported electrocatalysts at high overpotentials, at which the conversion of water to H₂ on carbon and the reduction of CO₂ to CO on Pd proceed at comparable rates, thereby leading to H₂ faradaic efficiencies (FEs) $\geq 50\%$.^{3, 4, 6} Alternatively, electrocatalysts featuring higher CO FEs as a result of their inhibited hydrogen evolution reaction (HER) activity⁷ could be designed by substituting carbon-supported catalysts with unsupported, carbon-free analogs.

In this regard, metal aerogels represent a unique opportunity as unsupported, self-stabilized three-dimensional nanonetworks enabling a high mass-normalized CO₂RR-activity and a suppression of the HER owing to the absence of a carbon support. Specifically, the aerogels' high surface areas and porosities⁸ render them exceptional (electro)catalyst,⁹ and they have additionally been shown to possess excellent electrochemical corrosion stability while diminishing the possibility of material loss due to corrosion of the carbon support.^{10, 11} As a result, aerogels have found application as electrocatalysts for O₂-reduction,^{10, 12, 13, 14} ethanol oxidation,^{11, 15} or CO₂-electroreduction, whereby SnPd,¹⁶ PdAg,¹⁷ AuPd,¹⁸ BiSn¹⁹ and PdCu²⁰ aerogels have been shown to yield high amounts of a single product (formate, CO or methanol), while Au²¹ and Pd²² aerogels displayed high FEs toward CO at high overpotentials.

Beyond this need for suppressing the HER, alloying of metals is commonly used²³ to influence the adsorption kinetics of reactants, intermediates and/or products to increase a catalyst's activity and selectivity toward the formation of a certain species. As a result, the alloying of two metals has often been applied in CO₂ electroreduction, whereby palladium has been previously alloyed with Cu,^{20, 24} Au,²⁵ Ag,²⁶ Ni,²⁶ Co,²⁶ In,²⁷ B,²⁸ and Pt.^{26, 29} In this last regard, Kortlever et al.²⁹ prepared PdPt alloy nanoparticles with various Pd:Pt atomic ratios (from 10:90 to 95:5) supported on carbon and found a maximum FE for formate production of $\approx 70\%$ at ≈ -0.45 V vs. the reversible hydrogen electrode (V_{RHE}) for an alloy composition of Pd₇₀Pt₃₀. On the other hand, Lee et al.²⁶ compared the CO₂RR selectivity of several carbon-supported Pd₈₀Me₂₀ (with Me = Ag, Cu, Ni, Co or Pt) alloys and found the Pd₈₀Pt₂₀ catalyst to yield significantly lower FEs toward CO than pure Pd. Furthermore, Cai et al.³⁰ investigated the CO₂RR-performance of bimetallic, carbon-supported nanoparticles consisting of co-deposited Pd and Pt, and found that Pd deposited on top of a Pt/C catalyst displayed a significantly larger formate selectivity and activity than Pt deposited on top of a Pd/C catalyst. Beyond these CO₂RR-focused studies, previous works by our groups extensively investigated PdPt aerogels from aqueous synthesis routes. Specifically, Liu et al.¹⁰ used bimetallic PdPt aerogels for the oxygen reduction reaction (ORR), while Oezaslan et al.^{31, 32} investigated how the aerogel's synthesis approach affects their structural homogeneity. Based on this experience and motivated by the promising formate FEs reported in Ref. 24 for PtPd-alloys, in this work, a series of PdPt aerogels with Pd:Pt atomic ratios ranging from 50:50 to 90:10 were prepared via a novel ethanolic synthesis approach.³³ We started by carefully assessing these aerogels' web thickness (systematically 6 ± 1 nm) and structural homogeneity using transmission electron microscopy (TEM), scanning electron microscopy (SEM) and powder X-ray diffraction (pXRD) measurements, as well as the alloying degree based on extended X-ray absorption fine structure (EXAFS) and energy-dispersive X-ray spectroscopy (EDX) measurements. These ex-situ characterizations were accompanied by electrochemical CO stripping measurements to infer the aerogels' electrochemical surface area (ECSA) and investigate their surface composition. Lastly, the bimetallic PdPt aerogels were employed as CO₂-

electroreduction catalysts and the observed reactivity trends were rationalized based on the bulk and surface composition results. In doing so, the aerogels' high activity toward the HER significantly reduced their selectivities toward both formate and CO, which we hypothesize is due to the aerogels' homogenous alloy nature, which entails the presence of Pt atoms on their surface with an enhanced activity toward H₂ evolution. Lastly, the Pd₁₀₀-aerogel was compared to a commercial, carbon-supported Pd nanoparticle (Pd/C) electrocatalyst, and its improved CO selectivity could be attributed to the lack of a carbon support.

2. EXPERIMENTAL SECTION

Bimetallic Aerogel synthesis

The mono- and bimetallic aerogels were synthesized using a combination of procedures described in detail by Georgi et al.³³ and Liu et al..¹⁰ A total of 1.6 mL (the ratio of Pd:Pt determined the final composition of the gel) of previously prepared ethanolic stock solutions of 0.05 mol·L⁻¹ PtCl₄ (Alfa Aesar; 99,99 %) and PdCl₂ (Alfa Aesar; 99,999 %) were typically diluted in 390 mL denaturated ethanol (Berkel AHK; 99 %; 1 % petroleum ether) at ambient conditions. A freshly prepared sodium borohydride solution was added quickly under vigorous stirring (450 rpm) of the solution. The amount of 50 mM NaBH₄ (Sigma-Aldrich; 99,99 %; granular) was used in a fixed ratio of metal ion equivalents to reduction agent equivalents ($n_{H^-} : n_{Me^+}$) of 12. After addition, the solution was stirred further for 30 s followed by leaving the solution overnight for 16 hours at room temperature until a black voluminous gel precipitate was formed on the bottom of the reaction vessel. The gel was collected and washed for a minimum of eight times with ethanol (Berkel AHK; 99 %; 1 % petroleum ether) to remove remaining residues. The resulting solvogels were transferred to aerogels via supercritical drying (13200J0AB, Spi Supplies) with CO₂ at 45 °C and 105 bar in an autoclave. NaBH₄, PtCl₄ and PdCl₂ were stored under inert atmosphere. The precise reactant and solvent volumes used to prepare each aerogel composition can be found in Table S1.

1 Characterization of the aerogels

2 Microscopic characterization

3 Basic structural analysis of the aerogels was performed by two different transmission electron
4 microscopes (TEM). These were a *JEOL/EO JEM- 1400plus* (120 kV) equipped with a LaB₆ cathode and
5 a *LIBRA 200* (Zeiss, 200 kV). The web thickness distribution (WTD) of each gel was obtained by
6 measuring the thickness of 200 strand-spots of a gel in a high-magnification TEM image using the
7 software *ImageJ*. Using this parameter, theoretically expected ECSA values ($ECSA_{WTD}$) were calculated
8 assuming that the aerogel geometry can be assimilated to a perfect continuous cylinder, from:

$$9 \quad ECSA_{WTD} = \frac{2 \pi \cdot \left(\frac{d_{aerogel}}{2} \right) \cdot L_{aerogel}}{m_{electrode}} \quad (1)$$

10

11 Therein, $d_{aerogel}$ is the mean web thickness of the aerogel as inferred from TEM, $m_{electrode}$ the mass of
12 the aerogel drop-casted onto the electrode, and $L_{aerogel}$ is the length of the approximated aerogel cylinder,
13 which can be calculated via:

14

$$15 \quad L_{Aerogel} = \frac{\frac{m_{electrode}}{\rho_{metal}}}{\pi \cdot \left(\frac{d_{aerogel}}{2} \right)^2} \quad (2)$$

16

17 where ρ_{Metal} is the stoichiometrically-weighed aerogel density based on the composition of the aerogels
18 and the densities of Pt (21.45 g·cm³) and Pd (11.99 g·cm³). Substituting Equation 2 into 1 one gets

19

$$ECSA_{WTD} = \frac{4}{\rho_{metal} \cdot d_{aerogel}} \quad (3)$$

enabling simple calculation of the expected ECSA. The three-dimensional porous structure as well as the element composition of the material were analyzed using a scanning electron microscope (SEM) FESEM SU8020 by Hitachi (2 kV, 10 μ A) coupled with a Silicon Drift Detector 80 X-Max^N from Oxford Instruments for bulk energy-dispersive X-ray spectroscopy (EDX). High-angle annular dark-field scanning transmission electron microscopy (HAADF-STEM) imaging combined with spectrum imaging analysis based on energy-dispersive X-ray spectroscopy (EDX) were performed at an accelerating voltage of 200 kV with a Talos F200X microscope equipped with an X-FEG electron source and a Super-X EDX detector system (FEI). Before STEM analysis, the specimen mounted in a high-visibility low-background holder was placed for 2 s into a Model 1020 Plasma Cleaner (Fischione) to remove potential contaminations.

X-ray diffraction

Powder X-ray diffraction (pXRD) measurements were performed on a Smartlab Rigaku system. The measurements were carried out for 2 θ angles between 5 and 90 ° using a copper rotating anode (Cu K $_{\alpha}$ = 1.5406 Å), a Cu K $_{\beta}$ filter, and a Rigaku HyPix3000 detector. All measurements were performed in Bragg-Brentano mode with the Cu-source set to 200 mA and 45 kV.

Ex-situ extended X-ray absorption fine structure measurements

X-ray absorption spectroscopy experiments were carried out at the SuperXAS (X10DA) beamline of the Swiss Light Source (SLS). Ex-situ spectra were recorded for 5 minutes using quickXAS at the Pd K-edge (24.350 keV) and Pt L₃-edge (11.563 keV) in transmission mode for all Pd- and Pt-containing samples, respectively. For the measurements at the Pd-edge, the polychromatic beam from the 2.9 T bending magnet (the SLS operated at 400 mA and 2.4 GeV) was collimated by a Pt-coated mirror at 2.87 mrad and monochromatized by a liquid N₂-cooled Si(111) channel-cut monochromator at an oscillation frequency of 1 Hz. The beam was focused using a Pt-coated toroidal mirror giving a spot size of 1 x 0.2

mm. The sample was placed between two ionization chambers (15 cm long) filled with Ar and N₂ (1 bar each) to measure both the incident and transmitted beam intensity. In contrast, at the Pt L₃-edge, a Rh-coated collimating mirror at 2.9 mrad was used with a liquid N₂-cooled Si(111) channel-cut monochromator set to an oscillation frequency of 1 Hz, a Rh-coated double-focusing mirror set to a focal point of 1 mm x 0.2 mm on the sample, and ionization chambers filled with N₂ at 2.5 bar. A Pd- or Pt-foil were placed before a third ionization chamber for the measurements at the Pd K- or Pt L₃-edges, respectively, and their spectra were used as a reference for energy calibration, using the maximum of the first derivative of the reference spectrum to align all sample spectra measured at the corresponding edges. The data treatment and analysis including calibration, background correction, normalization, and fitting was carried out using both the ProQEXAFS software³⁴ and the Demeter software package.³⁵ Spectra in a k-range of 3 to 14 Å⁻¹ were Fourier-transformed and fitted in an R-range of 1 to 3.3 Å. The ICSD database for inorganic crystal structures was used to acquire structures of Pd (ICSD-257579), Pt (ICSD-243678), PdO (ICSD-29281), and PtO₂ (ICSD-30443) that were used for scattering path calculations using FEFF. The reference measurements of the Pd and Pt foils were used to obtain fits with a coordination number of 12 to yield mean amplitude reduction factors (0.805 vs. 0.858 for Pd vs. Pt, respectively) used for the fitting of the sample spectra at the Pd K-edge and Pt L₃-edge, respectively.

Electrochemical measurements

Ink preparation

Inks of the aerogels were prepared individually for RDE and GC cell experiments aiming at metal loadings of 50 vs. 100 µg·cm⁻², respectively. A weighed amount of aerogel powder (≈ 2 mg) was dispersed in ultrapure water (18.2 MΩ·cm, ELGA Purelab Ultra) with the amount of water adjusted to be able to dose the desired loadings using drops of 20 or 100 µl for RDE vs. GC cell electrodes, respectively. Thereafter, an aliquot of Nafion perfluorinated resin solution (Sigma-Aldrich, 5 %) in the amount required to yield a Nafion-to-metal mass ratio of 0.2 was added to the same amount of water in a separate vial and

1 thoroughly mixed by shaking. The aerogel ink was carefully ultrasonicated (VWR USC100T) for a
2 maximum of 90 seconds until a homogenous dark grey ink was yielded. Drop casting for both RDE- and
3 GC-cell electrodes was carried out in two steps, in which the aerogel ink was drop cast and dried first and
4 a Nafion layer was added in a second step using the previously diluted resin solution. For the GC cell
5 electrodes, a previously described⁴ custom-built drop-casting setup was used. While RDE electrodes were
6 dried under N₂ flow, the GC cell electrodes were dried in a desiccator under reduced pressure. Aerogel
7 inks were resonicated a maximum of 3 times for 10 seconds and thereafter discarded. The process of
8 electrode preparation for GC electrodes for 20 % Pd/C (Premetek P30A200, Lot No. 100237) was very
9 similar and the Pd loading was kept at 100 $\mu\text{g}_{\text{Pd}}\cdot\text{cm}^{-2}$. However, a Nafion-to-carbon mass ratio of 0.2 was
10 used with a H₂O-to-isopropanol volume ratio of 70:30 with longer sonication times of 15 minutes and
11 drop-casting in a single drop of 25 μL .

12

13 Electrolyte preparation

14 For the preparation of the 0.5 M potassium bicarbonate electrolyte, 12.515 g of KHCO₃ (Honeywell,
15 99.95 % trace metals basis) were dissolved with ultrapure water to give 250 mL of solution. The measured
16 pH (Metrohm 913 pH meter with Metrohm Unitrode 6.0258.010) of the KHCO₃ electrolyte when
17 saturated with CO₂ (Messer AG, 5.5 quality), was repeatedly found to be 7.3. The 0.5 M potassium
18 phosphate buffer (K₂HPO₄/KH₂PO₄-buffer) was therefore set to this pH when saturated with N₂ (Carbagas
19 AG, 6.0 quality). This was achieved by mixing 17.146 g of di-potassium hydrogen phosphate (K₂HPO₄,
20 Merck LiChropur, anhydrous, 99.999 %) and 3.615 g potassium dihydrogen phosphate (KH₂PO₄, Merck,
21 LiChropur, anhydrous, 99.999 %) in 250 mL of ultrapure water.

22

23 Rotating disk electrode measurements

24 Thin-film rotating disk electrode (RDE) voltammetry³⁶ was used to determine the ECSA via H_{upd} and CO
25 stripping as well as to investigate the CO stripping characteristics of the aerogels depending on their

1 composition. The electrodes were prepared using the above-described two-step drop-casting of an ink
2 onto a mirror-polished, 5 mm diameter glassy carbon disk (HTW Hochtemperatur-Werkstoffe). The
3 glassy carbon disk was inserted in a PTFE RDE tip (E5TQ, Pine Research) and screwed into a shaft
4 (AFE6M, Pine Research) which was mounted into a rotation controller (Pine Research). The electrode
5 was thereafter inserted into a custom glass cell (Schmizo AG) with a gold mesh counter electrode (Advent
6 Research Materials) and an Ag/AgCl reference electrode (Harvard Apparatus, LF-1, filled with 3.4 M
7 KCl electrolyte and stored in a sealed vial partially filled with a 3 M KCl solution) pre-calibrated vs. the
8 RHE scale in the same electrolyte and held in individual glass compartments separated by glass frits
9 (Ametek G0300, 4 mm diameter). All electrodes were connected to the potentiostat (BioLogic, VSP-300),
10 while gas saturation was achieved by inserting a glass bubbler into the custom-made glass cell. The glass
11 cell and all other glass compartments were cleaned overnight in a piranha solution consisting of one part
12 H₂O₂ (30 %, Merck EMSURE) and three parts H₂SO₄ (96%, Merck Suprapure), subsequently washed
13 with ultra-pure water (18.2 MΩ·cm, ELGA Purelab Ultra) multiple times and thereafter boiled a minimum
14 of three times in ultrapure water.

15 CO stripping was carried out in RDE on electrodes conditioned by recording a minimum of ten CVs at
16 100 mV·s⁻¹, followed by five CVs at 50 mV·s⁻¹, two CVs at 20 mV·s⁻¹ and one CV at 10 mV·s⁻¹ between
17 0.05 and 1.25 V_{RHE}. Thereafter, the potential was held for 30 minutes at 0.4 or 0.1 V_{RHE} using a rotation
18 rate of 1600 rpm with the previously N₂-saturated solution being purged with CO for five minutes
19 followed by N₂ purging for 25 minutes. Subsequently, a linear sweep was run from the holding potential
20 to the negative inversion potential (0.05 V_{RHE}) and then positively to 1.25 V_{RHE} at 20 mV·s⁻¹. This sweep
21 was followed by two cycles in between 0.05 and 1.25 V_{RHE}. A specific CO stripping charge of
22 2·205 μC·cm_{Pd}⁻² was used to calculate the ECSA.³⁷

23

24

25

CO₂ electroreduction measurements

The selectivity and partial current density of the aerogels for CO₂ reduction were investigated using a custom online GC cell setup. A detailed description of the setup and measurement procedure was explained by Diercks et al.⁴. Therein, the drop casted-upon glassy carbon plate is inserted in the GC cell consisting of two polyether ether ketone (PEEK) compartments separated by a perfluorosulfonic acid membrane (Chemours, Nafion XL). The cell is filled with 3 mL CO₂ pre-saturated KHCO₃ and closed. During the measurement, CO₂ is continuously flowed at 10 mL·min⁻¹ via two mass flow controllers (Bronkhorst, IN-FLOW F201-CI) from the bottom of the cell while the cathode product gas stream is led through a homogenization volume (Swagelok, SS-4CD-TW-50) and sampled in five-minute intervals using an online gas chromatograph (SRI Instruments, 8610C).

Further gas saturation of both electrolyte compartments was carried out for five minutes, after which electrochemical impedance spectroscopy was recorded in between 1 MHz and 1 Hz applying a 10 mV perturbation at the open-circuit potential (OCP) to obtain a Nyquist plot from which the corresponding high-frequency resistance (HFR) was derived. Subsequently, this HFR was used for digital iR-compensation of 85 % for all following electrochemical measurements. The remaining 15 % of the HFR was manually corrected after the experiment during data treatment. The conditioning of the electrodes was carried out by recording 10 cyclic voltammograms (CVs) at 100 mV·s⁻¹, five CVs at 50 mV·s⁻¹, and one CV at 10 mV·s⁻¹ between 0.05 and 1.3 V_{RHE}. This was followed by a one-hour chronoamperometry measurement at a set potential, while online gas-product analysis was carried out using the GC. Thereafter, the catholyte was extracted and diluted for later analysis using ion-chromatography (Metrohm, 882 Compact IC plus) to infer the formate content. The anolyte as well as the working electrode were discarded (with the glassy carbon plate being repolished) and the cell disassembled to replace the working electrode to measure the subsequent potential using the above-described procedure.

3. RESULTS AND DISCUSSION

Aerogels' microscopic characterization

The aerogels' (nano-)structure was first inspected by scanning electron microscopy (SEM) and transmission electron microscopy (TEM), whereby the images acquired with the latter technique were used to infer the aerogels' web thickness distribution (WTD). A representative example of these images and the corresponding WTD for the as-prepared Pd₇₀Pt₃₀ aerogel are provided in Figure 1, while corresponding images for all other aerogel compositions can be found in Figures S1 to S6. While the SEM images clearly show a highly porous structure formed by a three-dimensional web of individual nanoparticle strings, the TEM reveals that this nanochain network consists of individual nanoparticles whose web thickness variation is featured in the WTD in Figure 1B. The aerogels' web thicknesses were found to be constant within the error of the method over the entire range of synthesized compositions and, as listed in Table 1, are equal to $\approx 6 \pm 1$ nm. Therefore, particle size effects on the selectivity trends reported below (and previously found for Pd-nanoparticles in CO₂RR-studies)^{5, 38} can be ruled out. Notably, these average web thicknesses allowed us to infer corresponding, WTD-based electrochemical surface areas (ECSAs) using Equation 3 in the Experimental section below and that are displayed (labeled as ECSA_{WTD}) in Table 1.

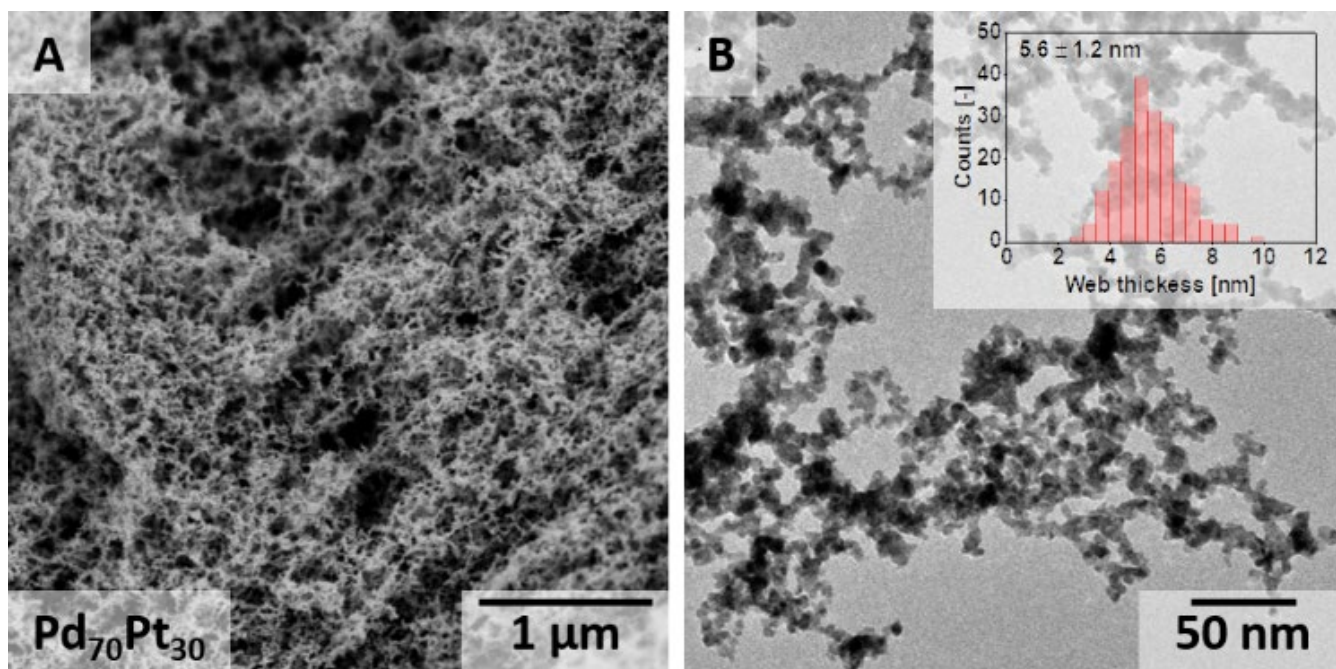


Figure 1. Representative scanning electron microscopy (SEM, A) and transmission electron microscopy (TEM, B) images of the pristine Pd₇₀Pt₃₀ aerogel, along with the corresponding web thickness distribution (see inset in B).

Additionally, the element distribution along the aerogel's necklace was investigated using EDX coupled with High Angle Annular Dark Field – Scanning Transmission Electron Microscopy (HAADF-STEM). Representative EDX element distribution maps of the Pd₇₀Pt₃₀ sample are shown in Figures 2A to 2D, while for the remaining PdPt compositions, equivalent images are displayed in Figures S7 to S10. Besides the HAADF-STEM image in Figure 2A, the superimposed Pd-Pt element distribution, as well as the single Pt and Pd maps, are plotted in Figures 2B, 2C, and 2D, respectively. These EDX-based element maps indicate a homogenous distribution (considering a resolution of the measurement of ≈ 1 nm) of both elements within the aerogel's particles, with no signs of significant segregation of Pd or Pt along the aerogels' web structure. Moreover, the aerogels' nominal Pd:Pt atomic ratios were found to agree well with those featured by the final materials, as indicated by the atomic ratios inferred from EDX-based compositional measurements in the SEM at 12 individual spots of each aerogel, and are listed in Table 1, for which the average deviation was found to be ≤ 1 at.-%.

Table 1. Summary of the aerogels' properties inferred from various characterization techniques. Pt:Pd atomic ratios derived from SEM-based EDX spot measurements at 12 different locations, crystallite sizes inferred from XRD using the Scherrer equation, TEM-derived average web thicknesses and corresponding theoretical surface areas (ECSA_{WTD}), along with the actual electrochemical surface areas inferred from the H_{upd} or CO stripping charges derived from electrochemical measurements ($\text{ECSA}_{\text{Hupd}}$ vs. $\text{ECSA}_{\text{CO},0.1\text{V}}$, respectively, whereby the latter was inferred using a CO-dosing potential of 0.1 V_{RHE} – see Experimental Section for details).

Material	EDX Composition	$d_{\text{Web, TEM}}$ [nm]	Crystallite size ^[a] [nm]	$\text{ECSA}_{\text{WTD}}^{\text{[b]}}$ [m ² ·g ⁻¹]	$\text{ECSA}_{\text{Hupd}}$ [m ² ·g ⁻¹]	$\text{ECSA}_{\text{CO},0.1\text{V}}$ [m ² ·g ⁻¹]	$\text{ECSA}_{\text{CO},0.1\text{V}}/\text{ECSA}_{\text{WTD}}$ [%]
Pt ₁₀₀	-	6.0 ± 1.3	4.9	31	23 ± 2	21 ± 2	66
Pd ₅₀ Pt ₅₀	Pd _{55.4} Pt _{44.6}	5.5 ± 1.1	4.6	43	35 ± 1	30 ± 1	69
Pd ₆₀ Pt ₄₀	Pd _{63.5} Pt _{36.5}	5.5 ± 1.2	4.0	46	36 ± 2	30 ± 4	66
Pd ₇₀ Pt ₃₀	Pd _{72.2} Pt _{27.8}	5.6 ± 1.2	4.1	48	47 ± 3	40 ± 3	82
Pd ₈₀ Pt ₂₀	Pd _{82.2} Pt _{17.8}	6.2 ± 1.0	3.5	47	45 ± 2	37 ± 1	80
Pd ₉₀ Pt ₁₀	Pd _{90.5} Pt _{9.5}	6.4 ± 1.7	3.5	48	43 ± 2	36 ± 3	75
Pd ₁₀₀	-	6.2 ± 1.0	4.1	54	53 ± 1	40 ± 1	74

[a] As extracted from X-ray diffractograms' broadened 111 peaks at a 2θ value of ≈ 40 ° using the Scherrer equation.

[b] Calculated based on the assumption that the aerogels can be assimilated to infinite cylinders of diameter equal to d_{web} and density (ρ) equal to the average of those of Pt and Pd weighed for the atomic compositions inferred from the EDX measurements (i.e., $\text{ECSA}_{\text{WTD}} = 4/(\rho \cdot d_{\text{web}})$ – see Equations 1 and 2 in the Experimental Section).¹³

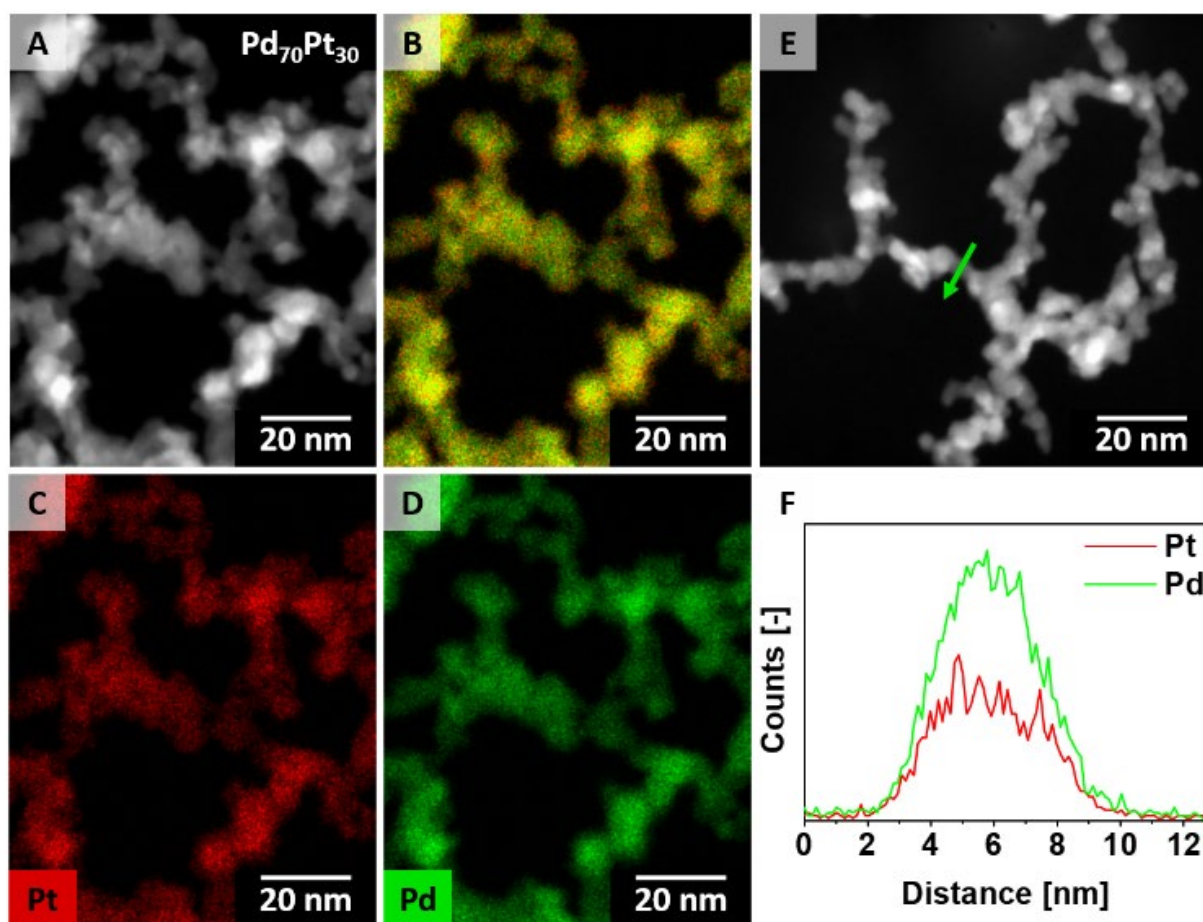


Figure 2. High-angle annular dark-field scanning transmission electron microscopy (HAADF-STEM) image of the $\text{Pd}_{70}\text{Pt}_{30}$ aerogel (A), superimposed Pt-Pd element distribution based on energy-dispersive X-ray spectroscopy (EDX) analysis (B) and single element distribution maps for Pt (C) and Pd (D) as well as a HAADF-STEM image (E) indicating the location and direction of the EDX line scan (F).

To further understand the aerogels' element distribution, we also recorded EDX line scans across their webs' diameter. A representative example of these results for the $\text{Pd}_{70}\text{Pt}_{30}$ sample can again be found in Figures 2E and 2F, which display the HAADF-STEM image with the location and direction of the line scan and the corresponding compositional information derived from it, respectively. Notably, the Pd:Pt ratio across the web diameter appears relatively constant and no indications of core-shell formation and/or of element segregation are observed.

In summary, the results derived from the EDX analysis point at a homogeneous distribution of the Pt and Pd atoms in all PdPt bimetallic aerogels.

Assessing the aerogels' alloying quality with X-ray diffraction and X-ray absorption spectroscopy

To investigate the alloying extent and crystallinity of the aerogels, XRD measurements were carried out. The acquired XRD patterns shown in Figure 3 display all the characteristic diffraction peaks expected for Pd and Pt in the face-centered cubic (fcc) lattice, as featured in the ICSD database.³⁹ Furthermore, no diffraction maxima assignable to side phases or oxides of either metal are found in the aerogels' XRD patterns. Apart from a minimal step feature at a 2θ value of $\approx 56^\circ$, which we assign to a measurement artefact, no significant shifts in the Bragg angles were found across the range of pure and bimetallic aerogels, as one can expect based on the very similar lattice parameters of both metals. As a result of this, the analysis of the diffraction patterns becomes very difficult³² and the alloy composition cannot be reliably inferred using Vegard's law.^{14, 40} However, the diffractograms' broadened 111 reflexes at a 2θ value of $\approx 40^\circ$ were used to infer the corresponding crystallite size using the Scherrer equation,¹³ which yielded values within the range of 3.5 to 5 nm for all aerogel compositions, which are thereby slightly below the corresponding aerogels' web thicknesses (see Table 1).

This crystallographic information was complemented by EXAFS spectroscopy measurements of the pristine aerogels from which we inferred their bulk composition and alloying degree. A specific comparison of the normalized XAS spectra of the monometallic aerogels and the corresponding foils of the same metals can be found in Figures S11 and S12 for Pd and Pt, respectively. Additionally, an overview of all normalized spectra at the Pd K- and Pt L₃-edges are displayed in Figures S13 and S14, respectively. While the spectra of the monometallic aerogels are in good agreement with those of the respective metal foils (cf. Figures S11 and

S12), those of the alloyed aerogels feature a clear shift in the EXAFS as a function of the Pt- or Pd-content.

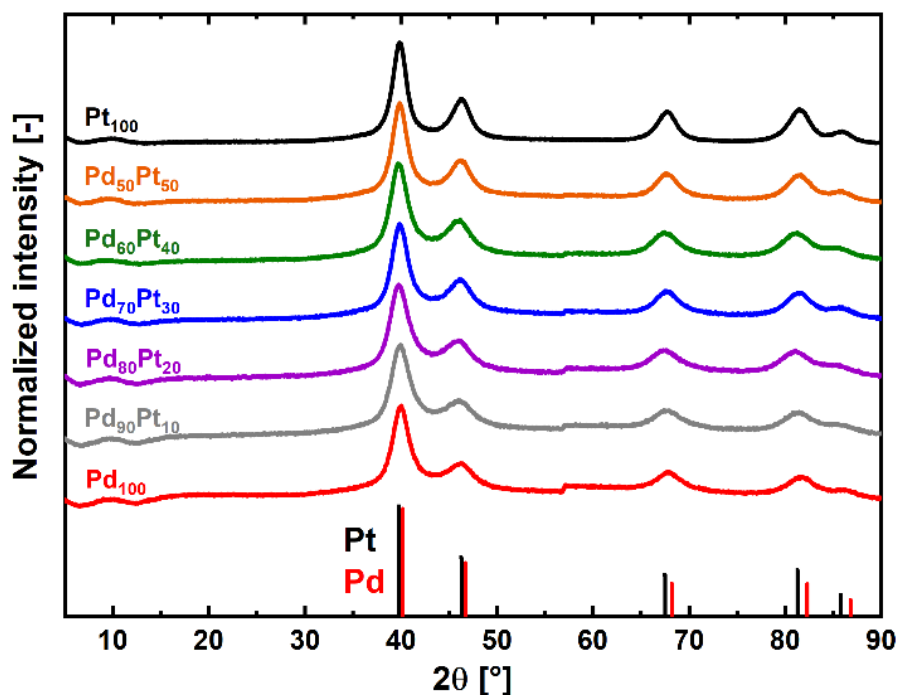


Figure 3. Powder X-ray diffractograms (pXRDs) of the as-prepared bi- and mono-metallic aerogels, along with the expected reflections for Pd ($a_{0,\text{Pd}} = 3.887 \text{ \AA}$, ICSD-77885⁴¹) and Pt ($a_{0,\text{Pt}} = 3.923 \text{ \AA}$, ICSD-76153⁴²) in an fcc lattice.

The exemplary EXAFS and corresponding, Fourier-transformed (FT-) spectra at both the Pd K- and Pt L₃-edges of the Pd₇₀Pt₃₀ aerogel are displayed in Figure 4, while the remaining EXAFS spectra of all other aerogels at their respective absorption edges can be found in Figure S15 and S16 (for the Pd K- vs. Pt L₃-edge, respectively). To assess the extent to which the two metals in the aerogels form an alloy, this FT-EXAFS data was firstly fitted with a scattering shell of the metal corresponding to the respective measurement edge (i.e. Pt at the Pt L₃-edge and Pd at the Pd K-edge). These and all subsequent fits are displayed in Figures 4, S15 and S16, and the corresponding R-factors (R_f) indicating the quality of the different fits are

additionally listed in Tables S2 and S3 and displayed in Figures S18 and S19 (whereby lower Rf values are synonymous of a higher quality fit). In the case of the monometallic aerogels, fitting with a single scattering path was found to lead to very good fits, while reasonably good Pd K-edge FT-EXAFS fits were obtained when applying this approach to the aerogels with a high Pd-content. On the other hand, none of the Pt L₃-edge EXAFS of the bimetallic materials could be fitted only considering a Pt-shell. Instead, fitting all PdPt aerogels FT-EXAFS with scattering paths for both Pd and Pt lead to a remarkable improvement of all fits at both edges, indicating a strong contribution to the EXAFS of Pd-Pt heterometallic bonds from which we conclude that these bimetallic materials can be described as homogenous bimetallic alloys, and not as intermixed monometallic phases.

This finding is in stark contrast to the results of previous studies by our groups on bimetallic PdPt aerogels prepared using gelation approaches different from the ethanolic route applied in this work (and described in the Experimental section), which entails spontaneous gelation at room temperature in ≤ 16 hours (overnight).³³ More precisely, a similar combined EXAFS and EDX analysis of PdPt aerogels prepared by an aqueous synthesis route entailing a significantly longer gelation time of 3 days at room temperature showed strong alloying behaviour between Pd and Pt atoms, however, significant variations in the local alloy composition were found along the nanochains.³¹ Additionally, in another aqueous synthesis route implying the separate preparation and subsequent mixing of Pd and Pt nanoparticles (two-step approach) followed by heating to 348 K for 5 to 10 hours, the materials were found consist of largely segregated Pd- and Pt-clusters.³²

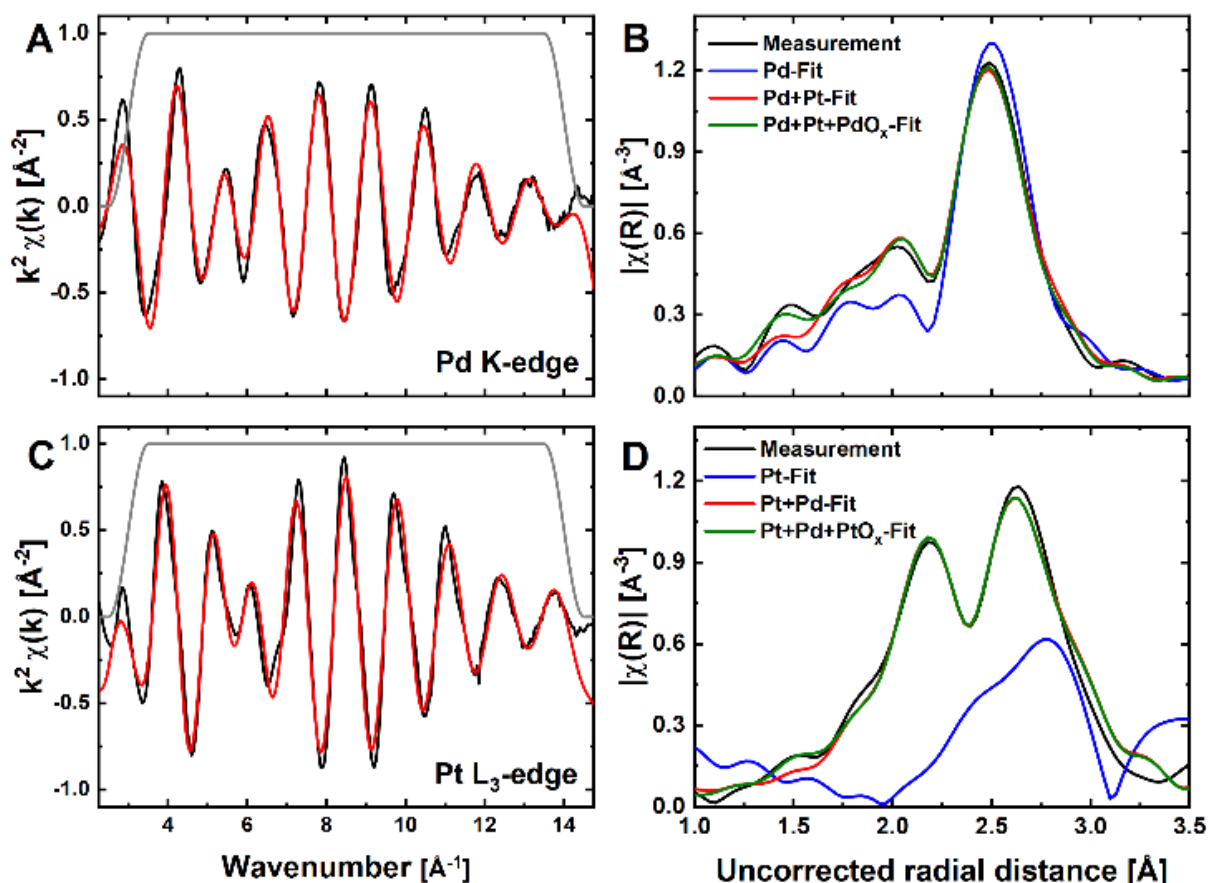


Figure 4. k^2 -space EXAFS (left) featuring the measured data and their respective fits (black vs. red lines, respectively, along with the wavenumber windows applied in the fits, (in grey) at the Pd K-edge ('A') and Pt L_3 -edge ('C') of the $\text{Pd}_{70}\text{Pt}_{30}$ aerogel, and the corresponding Fourier-transformed R-space spectra (right) with different scattering paths ('B' vs. 'D' for Pd K- vs. Pt L_3 -edge spectra, respectively).

We believe that these compositional discrepancies stem from the lower permittivity⁴³ and stabilization/reaction properties of NaBH_4 ⁴⁴ in the organic solvent (i. e. EtOH) used in the synthesis of the aerogels in this study (compared to the H_2O used in Refs 26a and 26b), which likely lead to faster reaction rates and a shorter gelation time that in terms results in the homogeneous mixing of Pd and Pt in these specific, bimetallic aerogels.

Furthermore, it is worth noting that all FT-EXAFS fits further improved upon the inclusion of

a metal-oxygen scattering path accounting for the R-space scattering signals at an uncorrected radial distance of ≈ 1.5 Å. Notably, we assign this oxide contribution to the formation of a (partial) Pd- and/or Pt-oxide layer on the aerogels' surface, which is exposed to air after the materials' synthesis and in the course of these ex-situ XAS measurements. Most importantly, as this improvement was found in all fits of the bimetallic aerogels at both the Pd K- and Pt L₃-edge, we hypothesize that on all bimetallic aerogels a non-negligible amount of both Pd and Pt is present on the surface. The final fits including these oxide scattering paths can be found in Tables S4 and S5 for the Pd K- and Pt L₃-edge spectra, respectively. Notably, the total coordination numbers were found to be between 9.4 ± 0.2 at the Pd K-edge and 9.0 ± 0.7 at the Pt L₃-edge across the entire range of the aerogel compositions (see Figure S19). Furthermore, the individual contributions of the Pd and Pt shells fitted at both absorption edges to the total coordination number are in qualitative agreement with the stoichiometry given by the synthesis as well as the composition inferred via EDX. In summary, EXAFS analysis confirms that the bimetallic aerogels consist of well-alloyed, homogeneously distributed, and non-segregated nanomaterials of controlled composition.

Electrochemical probing of the aerogels' surface composition

Following this microscopic and spectroscopic investigation, the aerogels were electrochemically characterized through rotating disk electrode (RDE) voltammetry measurements in N₂-saturated 0.5 M potassium phosphate buffer electrolyte with a pH of 7.3, as to match that of the potassium bicarbonate solution used in the subsequent CO₂RR measurements (see below). The cyclic voltammograms (CVs) recorded at a scan rate of $10 \text{ mV}\cdot\text{s}^{-1}$ are displayed in Figure S20, and a magnification of the hydrogen underpotential deposition (H_{upd}) region is displayed in Figure 5A. Notably, the H_{upd} features of the bimetallic aerogels are less distinct than those of the monometallic analogs, especially for the samples

with lower Pd-contents (i.e., Pd₅₀Pt₅₀ and Pd₆₀Pt₄₀), while those with higher Pd-contents (i.e., Pd₉₀Pt₁₀ and Pd₈₀Pt₁₀) show a distinct anodic peak at ≈ 0.30 V_{RHE} analogous to that featured by the pure Pd aerogel and thus indicative of a strong Pd contribution. Interestingly, this loss of distinct features in the CVs of the PdPt alloys with lower Pd-concentrations are in line with previous literature,^{29, 45} and such is also the case for the observation that the alloys' CV features are located at potentials in between those of the two metals constituting the alloy.⁴⁶

Finally, the aerogels' HER onset potential shifts linearly with their composition from the value of ≈ 75 mV_{RHE} observed for the Pd₁₀₀ aerogel to the ≈ 15 mV_{RHE} of Pt₁₀₀. As above, this observation is in line with previous findings.⁴⁵ Complementary to this, we also performed CO stripping measurements as a means to reliably quantify the aerogels' ECSA and further investigate their surface properties. In this regard, these measurements were carried out using CO-dosing potentials of 0.4 and 0.1 V_{RHE} for all materials, in an attempt to qualitatively assess the presence of Pt or Pd on their surface, since the CO coverage on Pt varies by ≈ 20 % among these two potentials but remains ≈ 100 % in the case of Pd.⁴⁷ Thus, representative CO stripping scans of all aerogels after holding the potential under CO-bubbling at 0.4 or 0.1 V_{RHE} are shown in Figures S21 vs. 5B, respectively. These CO-oxidation scans only feature one CO stripping peak, which renders the distinction between the contribution of surface Pt- or Pd-atoms to this oxidation process impossible.³¹

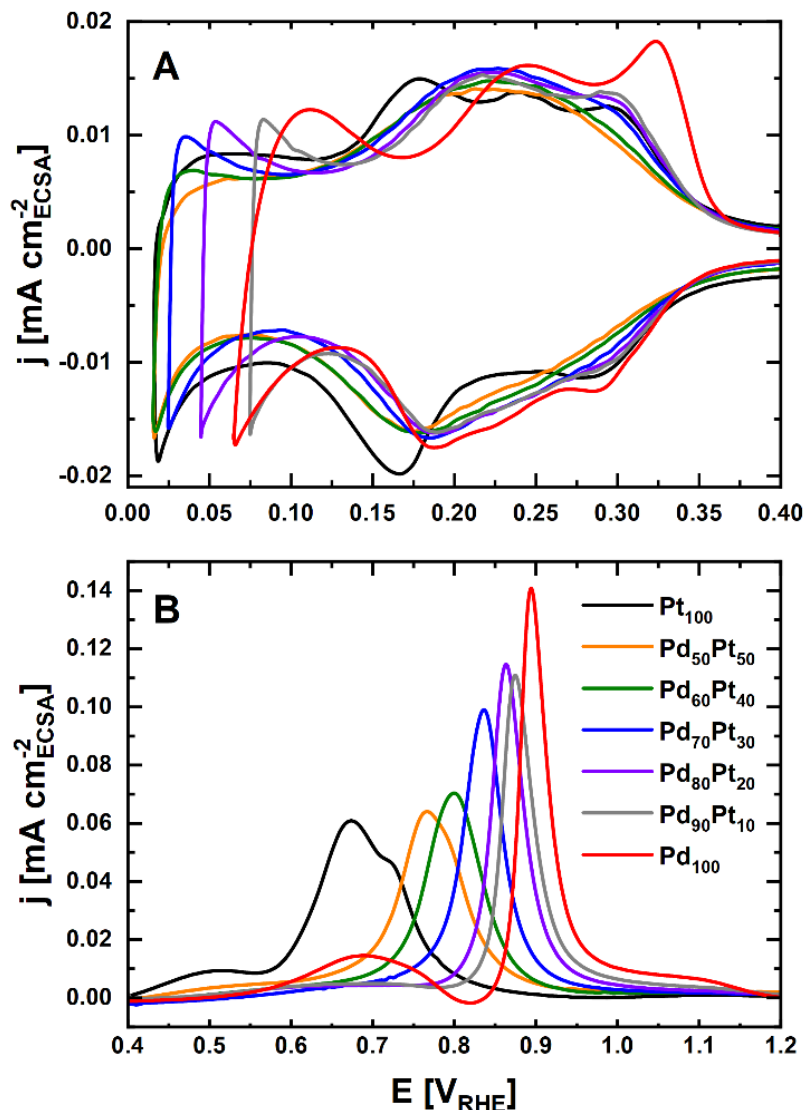


Figure 5. Hydrogen underpotential deposition (H_{upd}) areas of the cyclic voltammograms recorded on the aerogels in N_2 -saturated 0.5 M potassium phosphate buffer (K_2HPO_4/KH_2PO_4) at a scan rate of $10 \text{ mV}\cdot\text{s}^{-1}$ (A) and baseline-subtracted CO-oxidation scans recorded on all aerogels in N_2 -saturated 0.5 M potassium phosphate buffer (K_2HPO_4/KH_2PO_4) at a scan rate of $20 \text{ mV}\cdot\text{s}^{-1}$ after CO dosing at $0.1 \text{ V}_{\text{RHE}}$ (B).

Moreover, a clear trend is observed with regards to the effect of the aerogel composition on the position of this CO stripping peak, which progressively increases from ≈ 0.67 to $\approx 0.9 \text{ V}_{\text{RHE}}$ upon increasing the bulk Pd content from Pt_{100} to Pd_{100} (see Figure 6A). Notably, this peak position is not affected by the potential of CO-dosing (i.e., 0.4 or $0.1 \text{ V}_{\text{RHE}}$), as shown in Figure

6A. Several studies^{31, 32, 45, 48} reported a shift in the CO oxidation potential in dependence of the PdPt-composition similar to the one qualitatively observed here, in a trend that has been linked to the PdPt-surface composition.⁴⁹ We hence conclude that the surface composition is strongly dependent on the overall bulk composition and particularly highlight that these results indicate a lack of segregation between Pd and Pt within the surface of the aerogel.

Interestingly, the scans recorded for the Pt₁₀₀ aerogel feature a pre-peak for the holding potential of 0.1 V_{RHE} that is not found in the corresponding scan with a 0.4 V_{RHE} hold (see Figure S22). The absence of this pre-peak in the latter case is in agreement with the findings of Cuesta et al.⁴⁷ on polycrystalline Pt-surfaces, in which this voltammetric feature was assigned to Pt step sites that only get CO-poisoned at potentials < 0.35 V_{RHE}. In the case of Pd₁₀₀, such pre-peaks can be observed at both holding potentials, but the one following the hold at 0.1 V_{RHE} is comparatively much larger and most likely stems from the oxidation of hydrogen absorbed within the Pd-nanochains' bulk (see Figure S23). Therefore, it was not considered when calculating the charge ratios in Figure 6B. Meanwhile, the absence of these pre-peaks in the CO oxidation scans of all PdPt alloy compositions indicates that either CO is not adsorbed on step surface sites and/or that the aerogels' surface shifts the CO-oxidation potential toward values comparable to those expected for the terrace domains.

Additionally, Figure 6B displays the ratio between the CO stripping areas obtained with CO dosing potentials of 0.4 vs. 0.1 V_{RHE}. As discussed above, this ratio was roughly equal to unity for the pure palladium aerogel, while for the aerogel alloys with larger Pt-contents (i.e., Pd₅₀Pt₅₀ and Pd₆₀Pt₄₀), the higher holding potential led to a reduced CO oxidation charge (i.e., CO coverage) that comes increasingly close to the behavior displayed by the Pt₁₀₀ aerogel and previously found on polycrystalline Pt.⁴⁷ Additionally, in the case of the Pd₉₀Pt₁₀, Pd₈₀Pt₂₀, and Pd₇₀Pt₃₀ samples, these CO-oxidation charge ratios give values only slightly below unity, possibly indicating surface properties closer to those of pure Pd than what one would expect

from their bulk compositions. The above-discussed CO stripping and H_{upd} charges were further used to quantify the ECSA of the materials based on a minimum of three individual measurements, and the resulting values are listed in Table 1.

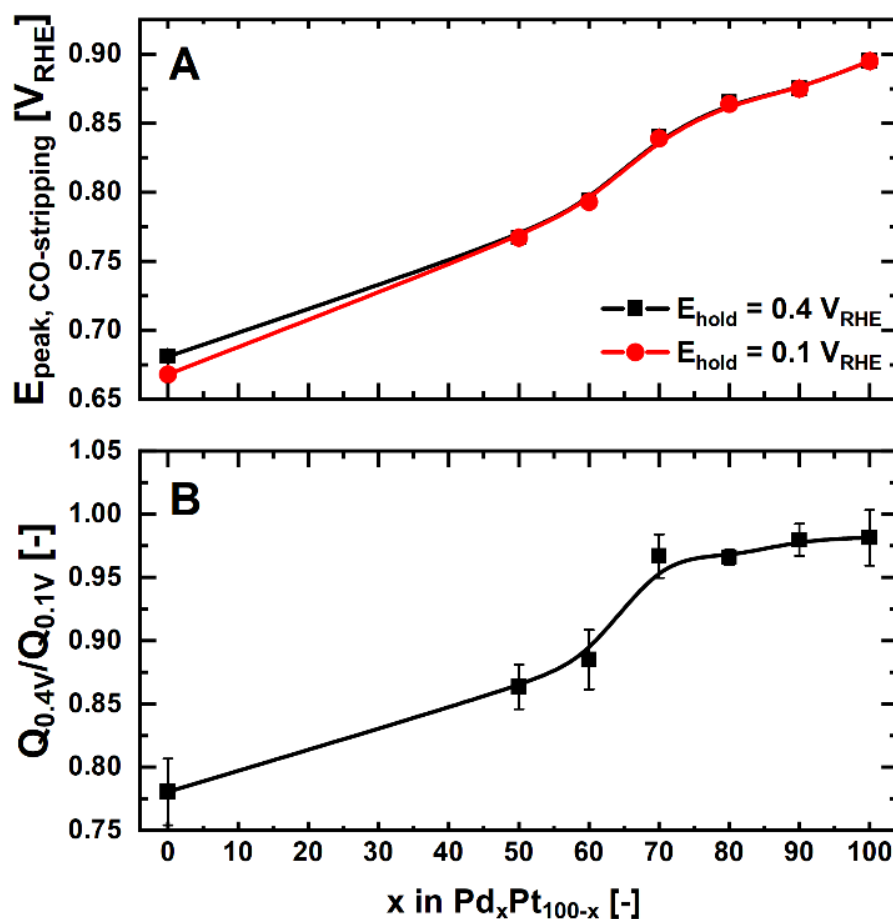


Figure 6. Effect of the aerogels' composition on the position of the CO stripping peak (A) and the ratio of the CO oxidation charges in CO stripping measurements with CO dosing potentials of 0.1 or 0.4 V_{RHE} (B).

As also summarized there, the ratio between the ECSAs inferred from the CO stripping measurements using a holding potential of 0.1 V_{RHE} and the afore-calculated theoretical surface areas based on the mean web thickness inferred via TEM (ECSA_{WTD}) is systematically within the range of ≈ 65 to ≈ 80 %. This implies that the fraction of the geometrical area inaccessible by the electrolyte (e.g., due to the connections among the aerogels' strings) remains roughly

equal among all materials included in this study. Most importantly, the results derived from this electrochemical characterization have revealed a strong dependence of the H_{upd} and CO stripping characteristics on the bulk composition. Considering the additional lack of any indications of surface segregation inferable from these surface-sensitive techniques, these results allow us to hypothesize that the aerogels' bulk composition is qualitatively retained within their surface. Notably, this possibility is consistent with the simultaneous presence of Pd and Pt atoms at the surface of all bimetallic materials inferred from our EDX and EXAFS results, whereby the inclusion of metal-oxide scattering paths indicative of (partially) oxidized surface atoms systematically led to an improvement of the EXAFS' fits.

Aerogels' CO₂ electroreduction performance

Following this assessment of all aerogels' bulk and surface composition, we proceeded to determine their CO₂-reduction activity through 1-hour potentiostatic measurements between - 0.1 and - 1.0 V_{RHE} in CO₂-saturated 0.5 M KHCO₃ using our custom-designed electrochemical cell.⁴ The potential-dependent FEs for all materials can be found in Figure 7A (for Pd₁₀₀) as well as Figures S22 to S27 (for Pt₁₀₀ and all PdPt alloys). Starting with the Pt₁₀₀ aerogel, Figure S24 shows that (as expected for this metal),⁵⁰ H₂ is the only product produced in a significant amount. Inversely, for the pure palladium aerogel (Pd₁₀₀, see Figure 7), we observe the expected high FE toward CO production at high overpotentials and CO₂RR selectivity toward formate at low overpotentials.^{3, 5} Meanwhile, for the PdPt alloy aerogels (see Figures S25 to S29) the formate and CO selectivities were found to progressively increase with decreasing Pt content, reaching maximum FEs of 47 vs. 22 % for CO vs. formate, respectively, for the Pd₉₀Pt₁₀ aerogel.

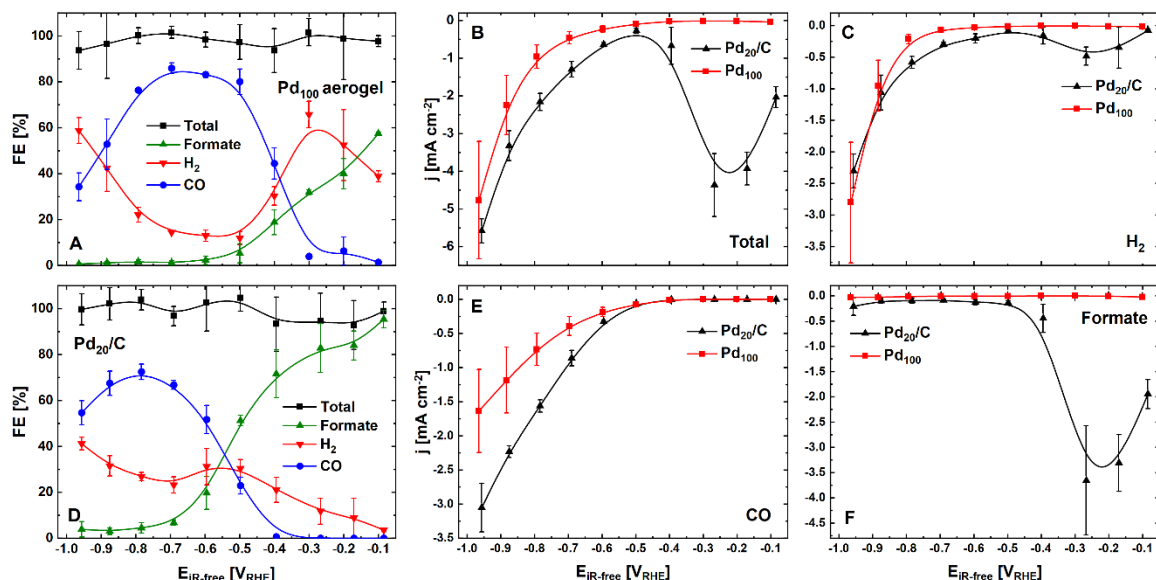


Figure 7. Product-specific and total faradaic efficiencies (FEs) upon CO₂ electroreduction on the Pd₁₀₀ aerogel (A) and Pd₂₀/C catalyst (D) with loadings of 100 $\mu\text{g}_{\text{Pd}}\cdot\text{cm}^{-2}$ and in CO₂-saturated 0.5 M KHCO₃, averaged over one hour holds at the specified, iR-corrected potentials, along with their respective total (B) and product-specific current densities for H₂ (C), CO (E) and formate (F). All reported values are averaged from three individual measurements, with the errors bars corresponding to the respective standard deviations. The data for Pd₂₀/C was adapted with permission from Reference [4]. Copyright CC BY 4.0 2021, the Electrochemical Society.

These selectivity trends can be further interpreted by analyzing the product-specific current densities plotted in Figure S30. There, the total current density (Figure S30A) at high overpotentials increases with an increase of the partial current density assignable to H₂ (see Figure S30B), which becomes dominant at these potentials. Complementarily, the partial current densities toward CO production (Figure S30C) only become significant at potentials < -0.5 V_{RHE}, and only the Pd₁₀₀ aerogel features a steady increase in partial CO current with increasing overpotential. As for formate production (Figure S30D), the Pd₁₀₀ aerogel shows

very low current densities at low overpotentials, while all other aerogels (and especially the Pd₈₀Pt₂₀ and Pd₉₀Pt₁₀ samples) display high activities toward formate production. However, due to the above-inferred presence of Pt atoms on the surface of these bimetallic PdPt materials, they are (already at these low overpotentials) much more active for hydrogen evolution than pure Pd, and thus they do not feature high overall selectivities toward formate and are outperformed by Pd₁₀₀ in this specific metric. We note in passing that we have not observed any signs of catalyst delamination even at the highest overpotentials and H₂-evolution current densities exceeding $-10 \text{ mA}\cdot\text{cm}^{-2}$; we hypothesize that this is caused by an enhanced evacuation of evolved gas bubbles through the thin catalyst layers yielded by these fully metallic aerogels (as compared to the thicker layers resulting from the use of C-supported catalysts).

The above-described selectivity trends are summarized in Figure 8, which features a detailed overview of the maximum FEs for formate and CO as a function of the alloy composition, including the previously discussed results by Kortlever et al.²⁹ (measured in CO₂-saturated 0.1 M KH₂PO₄/K₂HPO₄) and Lee et al.²⁶ (in CO₂-saturated 0.5 M KHCO₃). Interestingly, the FE vs. composition trends reported by Lee and coworkers for Pd₈₀Pt₂₀ and pure Pd nanoparticles supported on carbon qualitatively agree with our results for the equivalent Pd(Pt) aerogels. However, the selectivity differences between our work and the results reported by Kortlever et al.²⁹ are significant, and could tentatively stem from the homogenous structure of the aerogels inferred from the above characterization techniques. Notably, the presence of Pt-atoms within the aerogels' surfaces at all bimetallic compositions (qualitatively derived from the improvement of the EXAFS fits brought across by including a Pt-O scattering path and our electrochemical results, *vide supra*) is likely to lead to the observed promotion of the H₂-evolution over CO₂RR, since Pt is known to feature a remarkably high HER-activity.⁵¹ This effect seems to be dominant for the aerogels containing more than 30 at.-% Pt, for which

hydrogen production accounts for > 90 % of the FE across the entire potential range. In comparison, the PdPt catalysts employed by Kortlever et al.²⁹ may consist of Pd_{shell}-Pt_{core} structures devoid of surface Pt-atoms, as one would expect from multiple theoretical⁵² and experimental studies⁵³ therewith suggesting that the segregation of Pt toward the nanoparticles' bulk and the subsequent formation of a Pd-rich surface is energetically favored for such nanostructures.⁵⁴ Unfortunately, Kortlever et al.²⁹ did not present any results derived from techniques sensitive to the materials' elemental distribution, making the verification of this hypothetical explanation impossible. In this context, and in considering the crucial role of Pd-hydride on this metal's CO₂-reduction selectivity,^{3, 5, 6, 55} we acknowledge that the diminished hydride formation expected for PdPt alloys⁵⁶ may negatively affect their CO₂RR selectivities, whereas the core-shell materials possibly featured in the work by Kortlever et al.²⁹ could display enhanced hydride formation in their hypothesized Pd shells.

Beyond this highly tentative explanation, we ruled out that the aerogels' selectivity trends may result from a change of their surface composition during the CO₂RR measurement by performing CO stripping measurements on the Pd₇₀Pt₃₀ aerogel before and after CO₂ reduction for 1 hour at - 0.5 V_{RHE}. As shown in Figure S31, no shifts in the peak position and/or shape of these CO-oxidation scans were observed as a consequence of the CO₂RR measurement, from which we infer that the aerogel did not undergo any significant change in composition during the experiment.

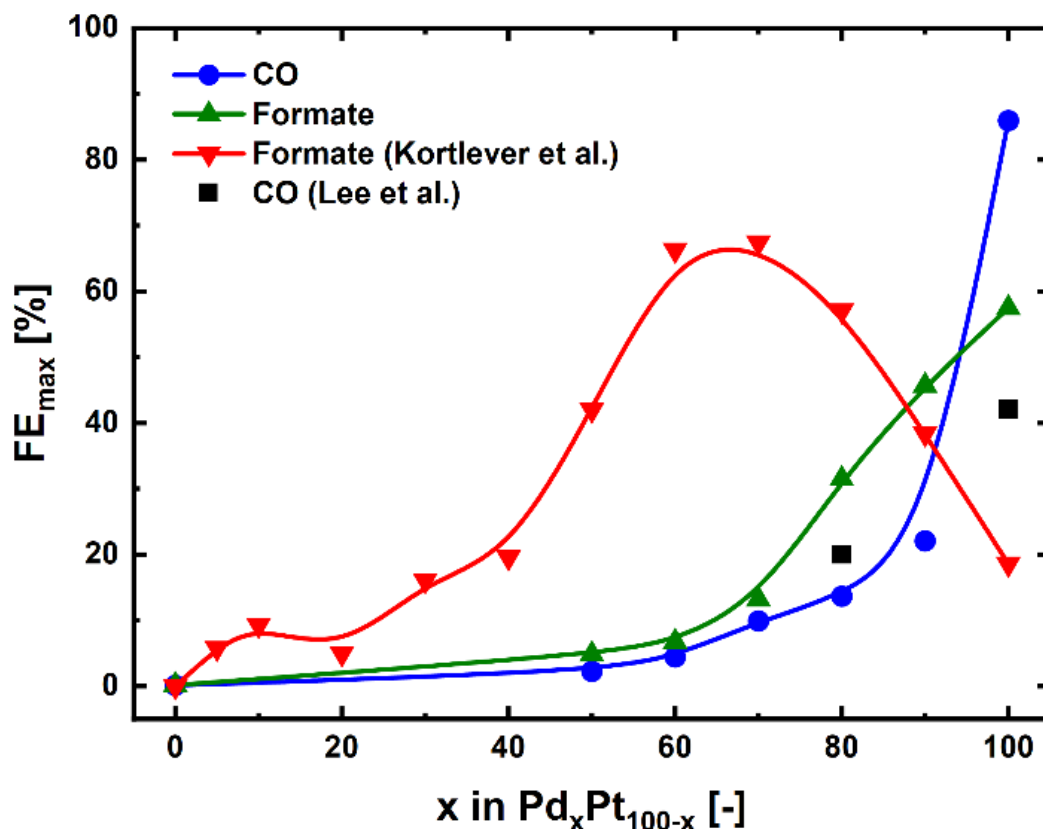


Figure 8. Maximum faradaic efficiency (FE) toward CO and formate production as a function of the Pd content in each aerogel, as well as the maximum FE toward formate on the PdPt/C catalyst synthesized by Kortlever et al.²⁹ and the corresponding FEs found for the two compositions employed by Lee et al.²⁶.

We finalize our study by assessing the effect of the aerogel's absence of a carbon support on the CO₂RR-product selectivity hypothesized at the beginning of our work. To this end, we compare the performance of the pure, Pd₁₀₀ aerogel with that of a 20 % Pd/C catalyst (with an average particle diameter of ≈ 4 nm)³⁷ previously tested in the same cell and identical conditions.⁴ This comparison unveils that both materials feature the distribution of the product selectivity with potential previously reported for resembling Pd nanostructures.³⁻⁵ On the other hand, the partial current densities toward CO and formate measured on both of these materials are ≈ 2 - to ≈ 5 -fold lower than those reported in the literature,^{3-5, 57} possibly due to differences in the cell design (and concomitant mass transport properties), electrolyte and/or catalyst

loadings used in our study as compared to those works. Beyond these differences, the comparison between the Pd₁₀₀ aerogel and Pd/C unveils that the aerogel's FE and partial current toward formate (maxing at $\approx 0.1 \text{ mA/cm}^2$ and $\approx 60 \%$, respectively) are significantly lower than those displayed by the Pd/C catalyst ($\approx 3 \text{ mA/cm}^2$ and $\approx 80 \%$ – see Figure 7A, D and F). In contrast, the potential-dependent CO-selectivity between -0.5 and $-0.8 \text{ V}_{\text{RHE}}$ is found to be significantly higher ($\approx 80 \%$) and extends over a broader potential range for Pd₁₀₀ as compared to the Pd/C catalyst. The same effect can be found when this comparison is carried out with regards to a Pd/C catalyst with a particle diameter of $\approx 6 \text{ nm}$ similar to the Pd₁₀₀ aerogel's web thickness.³⁸ Concomitantly, very low H₂ FEs are found on Pd₁₀₀ at these intermediate overpotentials when compared to the Pd/C catalyst (see Figure 7C), while below $-0.8 \text{ V}_{\text{RHE}}$ the activity toward hydrogen production dramatically increases and the selectivity drastically shifts toward H₂-evolution. Therefore, we hypothesize that the late onset of the hydrogen evolution reaction on the pure Pd₁₀₀ aerogel and its suppression at intermediate overpotentials is the result of this material's lack of a carbon support, which would in turn enable the observed increase in CO selectivity and confirm the advantages of unsupported aerogels that partially motivated this study. Hence, the Pd₁₀₀ aerogel is a promising catalyst for CO generation at high overpotentials, and future work should be devoted to upscale its synthesis and test its performance in CO₂-fed electrolyzers.⁵⁸

4. CONCLUSION

In this study, a series of unsupported, Pd-rich bimetallic PdPt aerogels was synthesized and characterized using microscopic techniques that revealed the aerogels' hierarchically porous web structure of consistent thickness across all PdPt compositions. Additionally, EDX, XRD, and EXAFS analyses showed the aerogels to consist of homogeneous alloys, with no indication of the formation of core-shell structures or of element segregation that one may have been expected based on previous literature on this bimetallic system. This lack of metal segregation effects at the surface level and the dependence of the number of surface Pt atoms proportional to the alloys' bulk composition was further confirmed by the aerogels' electrochemical characterization, with additional signs of the presence of surface Pt atoms within all bimetallic compositions being inferred based on the materials' EXAFS fits.

Finally, our CO₂ electroreduction selectivity tests showed an increased selectivity toward CO on the Pd₁₀₀ sample that is ascribable to the suppression of the HER at intermediate overpotentials caused by the absence of a carbon support. On the other hand, the faradaic efficiencies of the bimetallic PdPt aerogels toward formate and CO were found to be much lower than those reported in previous studies on seemingly analogous, bimetallic materials. We hypothesize that the homogenous alloy structure of these PdPt aerogels (as opposed to the Pd_{shell}Pt_{core} structure expected based on thermodynamical phase stability studies) is responsible for these differences since the presence of surface Pt-atoms leads to increased activities toward the HER and therewith diminished the corresponding selectivities toward CO₂RR products (CO and formate) across the entire potential range. Therefore, we suggest that careful consideration is necessary regarding the homogeneity and surface structure of bimetallic PdPt nanocatalysts to optimize their CO₂ electroreduction performance.

Supporting Information.

The supporting information is available free of charge at *–insert link here–*.

The SI contains further SEM, TEM, HAADF-STEM and EDX analysis as well as XAS spectra, EXAFS fits and EXAFS fitting data on the aerogels. Furthermore, additional electrochemical results and detailed CO₂ electroreduction selectivities for the PdPt aerogel alloys are reported.

AUTHOR INFORMATION

Corresponding Author

*Juan Herranz: juan.herranz@psi.ch

Author Contributions

Justus S. Diercks: Writing, Conceptualization, Measurements, Analysis, Interpretation.

Maximilian Georgi: PdPt aerogel synthesis, SEM and TEM measurements.

Juan Herranz: Conceptualization, Interpretation, Editing, Supervision.

Natasa Diklic: XRD measurements and analysis.

Piyush Chauhan: Electrochemical and XAS measurement support.

Adam H. Clark: XAS measurement and analysis support.

René Hübner: HAADF-STEM and EDX measurements.

Antoine Faisnel: CO₂RR selectivity measurements.

Qinhao Chen: CO₂RR selectivity measurements.

Maarten Nachtegaal: XAS measurement support.

Alexander Eychmüller: Supervision, Resources.

Thomas J. Schmidt: Conceptualization, Interpretation, Supervision, Resources.

All authors have given approval to the final version of the manuscript.

Funding Sources

Swiss Competence Center for Energy Research (SCCER) Heat & Electricity Storage

Swiss National Science Foundation (SNSF, grant 200020L_178737)

Deutsche Forschungsgemeinschaft (German Research Foundation) (DFG EY 16/18-2)

ACKNOWLEDGMENT

Funding of this project for PSI's Electrochemistry Laboratory by the Swiss Competence Center for Energy Research (SCCER) Heat & Electricity Storage and the Swiss National Science Foundation (SNSF, grant 200020L_178737) as well as for the Physical Chemistry group by the Deutsche Forschungsgemeinschaft (German Research Foundation) (DFG EY 16/18-2) are gratefully acknowledged. The authors thank Dr. Karl Hiekel and Dr. Nelli Weiß for their support with TEM measurements as well as Dr. Mauro Povia and Dr. Elena Marelli for their insights into XRD measurements. Lastly, the authors gratefully acknowledge the funding of TEM Talos by the German Federal Ministry of Education and Research (BMBF), Grant No. 03SF0451, in the framework of HEMCP and thank the SuperXAS beamline at the Swiss Light Source for the use of their facilities.

Notes

The authors declare no competing financial interest.

REFERENCES

- (1) Carattini, S.; Kallbekken, S.; Orlov, A. How to win public support for a global carbon tax. *Nature* **2019**, *565*, 289-291.
- (2) Durst, J.; Rudnev, A.; Dutta, A.; Fu, Y.; Herranz, J.; Kaliginedi, V.; Kuzume, A.; Permyakova, A. A.; Paratcha, Y.; Broekmann, P. Electrochemical CO₂ reduction—A critical view on fundamentals, materials and applications. *CHIMIA International Journal for Chemistry* **2015**, *69* (12), 769-776. Spurgeon, J. M.; Kumar, B. A comparative technoeconomic analysis of pathways for commercial electrochemical CO₂ reduction to liquid products. *Energy & Environmental Science* **2018**, *11* (6), 1536-1551, 10.1039/C8EE00097B. DOI: 10.1039/C8EE00097B.
- (3) Gao, D.; Zhou, H.; Cai, F.; Wang, D.; Hu, Y.; Jiang, B.; Cai, W.-B.; Chen, X.; Si, R.; Yang, F.; et al. Switchable CO₂ electroreduction via engineering active phases of Pd nanoparticles. *Nano Research* **2017**, *10* (6), 2181-2191. DOI: 10.1007/s12274-017-1514-6.
- (4) Diercks, J. S.; Pribyl-Kranewitter, B.; Herranz, J.; Chauhan, P.; Faisnel, A.; Schmidt, T. J. An Online Gas Chromatography Cell Setup for Accurate CO₂-Electroreduction Product Quantification. *Journal of The Electrochemical Society* **2021**, *168* (6), 064504. DOI: 10.1149/1945-7111/ac0363.
- (5) Rahaman, M.; Dutta, A.; Broekmann, P. Size-Dependent Activity of Palladium Nanoparticles: Efficient Conversion of CO₂ into Formate at Low Overpotentials. *ChemSusChem* **2017**, *10* (8), 1733-1741. DOI: 10.1002/cssc.201601778.
- (6) Sheng, W.; Kattel, S.; Yao, S.; Yan, B.; Liang, Z.; Hawxhurst, C. J.; Wu, Q.; Chen, J. G. J. E.; Science, E. Electrochemical reduction of CO₂ to synthesis gas with controlled CO/H₂ ratios. *Energy & Environmental Science* **2017**, *10* (5), 1180-1185.
- (7) Duan, C. C. Selective CO₂ electrohydrogenation. *Nature Catalysis* **2021**, *4* (4), 264-265, Editorial Material. DOI: 10.1038/s41929-021-00600-6.
- (8) Schneider, K.; Melnyk, I.; Hiekel, K.; Fery, A.; Auernhammer, G. K.; Eychmüller, A. Mechanical Characterization of Self-Supported Noble Metal Gel Monoliths. *The Journal of Physical Chemistry C* **2019**. DOI: 10.1021/acs.jpcc.9b08607. Herrmann, A.-K.; Formanek, P.; Borchardt, L.; Klose, M.; Giebeler, L.; Eckert, J. r.; Kaskel, S.; Gaponik, N.; Eychmüller, A. Multimetallic aerogels by template-free self-assembly of Au, Ag, Pt, and Pd nanoparticles. *Chemistry of Materials* **2014**, *26* (2), 1074-1083.
- (9) Ziegler, C.; Wolf, A.; Liu, W.; Herrmann, A. K.; Gaponik, N.; Eychmüller, A. Modern inorganic aerogels. *Angewandte Chemie International Edition* **2017**, *56* (43), 13200-13221.
- (10) Liu, W.; Rodriguez, P.; Borchardt, L.; Foelske, A.; Yuan, J.; Herrmann, A. K.; Geiger, D.; Zheng, Z.; Kaskel, S.; Gaponik, N.; et al. Bimetallic Aerogels: High-Performance Electrocatalysts for the Oxygen Reduction Reaction. *Angewandte Chemie International Edition* **2013**, *52* (37), 9849-9852.
- (11) Zareie Yazdan-Abad, M.; Noroozifar, M.; Modaresi Alam, A. R.; Saravani, H. Palladium aerogel as a high-performance electrocatalyst for ethanol electro-oxidation in alkaline media. *Journal of Materials Chemistry A* **2017**, *5* (21), 10244-10249, 10.1039/C7TA03208K. DOI: 10.1039/C7TA03208K.

- (12) Cai, B.; Henning, S.; Herranz, J.; Schmidt, T. J.; Eychmüller, A. Nanostructuring noble metals as unsupported electrocatalysts for polymer electrolyte fuel cells. *Advanced Energy Materials* **2017**, 7 (23), 1700548. Henning, S.; Herranz, J.; Gasteiger, H. A. Bulk-palladium and palladium-on-gold electrocatalysts for the oxidation of hydrogen in alkaline electrolyte. *Journal of The Electrochemical Society* **2015**, 162 (1), F178-F189. Henning, S.; Herranz, J.; Ishikawa, H.; Kim, B. J.; Abbott, D.; Kühn, L.; Eychmüller, A.; Schmidt, T. J. Durability of Unsupported Pt-Ni Aerogels in PEFC Cathodes. *Journal of The Electrochemical Society* **2017**, 164 (12), F1136-F1141.
- (13) Henning, S.; Kühn, L.; Herranz, J.; Durst, J.; Binninger, T.; Nachtegaal, M.; Werheid, M.; Liu, W.; Adam, M.; Kaskel, S.; et al. Pt-Ni Aerogels as Unsupported Electrocatalysts for the Oxygen Reduction Reaction. *Journal of The Electrochemical Society* **2016**, 163 (9), F998-F1003. DOI: 10.1149/2.0251609jes.
- (14) Henning, S.; Kühn, L.; Herranz, J.; Nachtegaal, M.; Hübner, R.; Werheid, M.; Eychmüller, A.; Schmidt, T. J. Effect of Acid Washing on the Oxygen Reduction Reaction Activity of Pt-Cu Aerogel Catalysts. *Electrochimica Acta* **2017**, 233, 210-217.
- (15) Liu, W.; Herrmann, A.-K.; Geiger, D.; Borchardt, L.; Simon, F.; Kaskel, S.; Gaponik, N.; Eychmüller, A. High-Performance Electrocatalysis on Palladium Aerogels. *Angewandte Chemie International Edition* **2012**, 51 (23), 5743-5747. DOI: <https://doi.org/10.1002/anie.201108575>.
- (16) Abdinejad, M.; Motlagh, M. K.; Noroozifar, M.; Kraatz, H. B. Electroreduction of carbon dioxide to formate using highly efficient bimetallic Sn-Pd aerogels. *Materials Advances* **2022**, 3, 1224.
- (17) Abdinejad, M.; Ferrag, C.; Hossain, M. N.; Noroozifar, M.; Kerman, K.; Kraatz, H. B. Capture and electroreduction of CO₂ using highly efficient bimetallic Pd-Ag aerogels paired with carbon nanotubes. *Journal of Materials Chemistry A* **2021**, 9, 12870-12877, Article; Early Access. DOI: 10.1039/d1ta01834e.
- (18) Du, R.; Jin, W.; Wu, H.; Hübner, R.; Zhou, L.; Xue, G.; Hu, Y.; Eychmüller, A. Rapid synthesis of gold-palladium core-shell aerogels for selective and robust electrochemical CO₂ reduction. *Journal of Materials Chemistry A* **2021**, 9 (32), 17189-17197, 10.1039/D1TA03103A. DOI: 10.1039/D1TA03103A.
- (19) Ma, T.; Wu, Z.; Wu, H.; Cai, W.; Wen, Z.; Wang, L.; Jin, W.; Jia, B. Engineering Bi-Sn Interface in Bimetallic Aerogel with 3D Porous Structure for Highly Selective Electrocatalytic CO₂ Reduction to HCOOH. *Angewandte Chemie* **2021**, 60 (22), 12554-12559.
- (20) Lu, L.; Sun, X.; Ma, J.; Yang, D.; Wu, H.; Zhang, B.; Zhang, J.; Han, B. Highly Efficient Electroreduction of CO₂ to Methanol on Palladium-Copper Bimetallic Aerogels. *Angewandte Chemie Int Ed* **2018**, 57 (43), 14149-14153. DOI: 10.1002/anie.201808964.
- (21) Chauhan, P.; Hiekel, K.; Diercks, J. S.; Herranz, J.; Saveleva, V. A.; Khavlyuk, P.; Eychmüller, A.; Schmidt, T. J. Electrochemical Surface Area Quantification, CO₂ Reduction Performance, and Stability Studies of Unsupported Three-Dimensional Au Aerogels versus Carbon-Supported Au Nanoparticles. *ACS Materials Au* **2022**, 2 (3), 278-292. DOI: 10.1021/acsmaterialsau.1c00067.
- (22) Li, Y.; Zhang, K.; Yu, Y.; Zhan, X.; Gui, J.; Xue, J.; Jin, X.; Gao, S.; Xie, Y. Pd homojunctions enable remarkable CO₂ electroreduction. *Chemical Communications* **2021**, 58 (3), 387-390, 10.1039/D1CC04780A. DOI: 10.1039/D1CC04780A.
- (23) Markovic, N. M. Interfacing electrochemistry. *Nature Materials* **2013**, 12 (2), 101-102. DOI: 10.1038/nmat3554.
- (24) Xie, J. F.; Chen, J. J.; Huang, Y. X.; Zhang, X.; Wang, W. K.; Huang, G. X.; Yu, H. Q. Selective electrochemical CO₂ reduction on Cu-Pd heterostructure. *Appl. Catal. B-Environ.* **2020**, 270, 8, Article. DOI: 10.1016/j.apcatb.2020.118864. Rahaman, M.; Kiran, K.; Montiel,

- I. Z.; Grozovski, V.; Dutta, A.; Broekmann, P. Selective-propanol formation from CO₂ over degradation-resistant activated PdCu alloy foam electrocatalysts. *Green Chem.* **2020**, *22* (19), 6497-6509, Article. DOI: 10.1039/d0gc01636e. Yin, Z.; Gao, D. F.; Yao, S. Y.; Zhao, B.; Cai, F.; Lin, L. L.; Tang, P.; Zhai, P.; Wang, G. X.; Ma, D.; et al. Highly selective palladium-copper bimetallic electrocatalysts for the electrochemical reduction of CO₂ to CO. *Nano Energy* **2016**, *27*, 35-43, Article. DOI: 10.1016/j.nanoen.2016.06.035.
- (25) Celorrio, V.; Quaino, P. M.; Santos, E.; Florez-Montano, J.; Humphrey, J. J. L.; Guillen-Villafuerte, O.; Plana, D.; Lazaro, M. J.; Pastor, E.; Fermin, D. J. Strain Effects on the Oxidation of CO and HCOOH on Au-Pd Core-Shell Nanoparticles. *ACS Catalysis* **2017**, *7* (3), 1673-1680, Article. DOI: 10.1021/acscatal.6b03237. Yuan, X. T.; Zhang, L.; Li, L. L.; Dong, H.; Chen, S.; Zhu, W. J.; Hu, C. L.; Deng, W. Y.; Zhao, Z. J.; Gong, J. L. Ultrathin Pd-Au Shells with Controllable Alloying Degree on Pd Nanocubes toward Carbon Dioxide Reduction. *Journal of the American Chemical Society* **2019**, *141* (12), 4791-4794, Article. DOI: 10.1021/jacs.8b11771. Zhu, S.; Qin, X.; Wang, Q.; Li, T.; Tao, R.; Gu, M.; Shao, M. Composition-dependent CO₂ electrochemical reduction activity and selectivity on Au-Pd core-shell nanoparticles. *Journal of Materials Chemistry A* **2019**, *7* (28), 16954-16961, 10.1039/C9TA05325E. DOI: 10.1039/C9TA05325E. Valenti, M.; Prasad, N. P.; Kas, R.; Bohra, D.; Ma, M.; Balasubramanian, V.; Chu, L.; Gimenez, S.; Bisquert, J.; Dam, B.; et al. Suppressing H₂ Evolution and Promoting Selective CO₂ Electroreduction to CO at Low Overpotentials by Alloying Au with Pd. *ACS Catalysis* **2019**, *9* (4), 3527-3536. DOI: 10.1021/acscatal.8b04604.
- (26) Lee, J. H.; Kattel, S.; Jiang, Z.; Xie, Z.; Yao, S.; Tackett, B. M.; Xu, W.; Marinkovic, N. S.; Chen, J. G. Tuning the activity and selectivity of electroreduction of CO₂ to synthesis gas using bimetallic catalysts. *Nature Communications* **2019**, *10* (1), 3724. DOI: 10.1038/s41467-019-11352-0.
- (27) Pavesi, D.; Ali, F. S. M.; Anastasiadou, D.; Kallio, T.; Costa Figueiredo, M.; Gruter, G.-J. M.; Koper, M. T. M.; Schouten, K. J. P. CO₂ electroreduction on bimetallic Pd-In nanoparticles. *Catalysis Science & Technology* **2020**, *10* (13), 4264-4270, 10.1039/D0CY00831A. DOI: 10.1039/D0CY00831A.
- (28) Jiang, T.-W.; Zhou, Y.-W.; Ma, X.-Y.; Qin, X.; Li, H.; Ding, C.; Jiang, B.; Jiang, K.; Cai, W.-B. Spectrometric Study of Electrochemical CO₂ Reduction on Pd and Pd-B Electrodes. *ACS Catalysis* **2021**, *11* (2), 840-848. DOI: 10.1021/acscatal.0c03725.
- (29) Kortlever, R.; Peters, I.; Koper, S.; Koper, M. T. M. Electrochemical CO₂ Reduction to Formic Acid at Low Overpotential and with High Faradaic Efficiency on Carbon-Supported Bimetallic Pd-Pt Nanoparticles. *ACS Catalysis* **2015**, *5* (7), 3916-3923. DOI: 10.1021/acscatal.5b00602.
- (30) Cai, F.; Gao, D.; Si, R.; Ye, Y.; He, T.; Miao, S.; Wang, G.; Bao, X. Effect of metal deposition sequence in carbon-supported Pd-Pt catalysts on activity towards CO₂ electroreduction to formate. *Electrochemistry Communications* **2017**, *76*, 1-5. DOI: <https://doi.org/10.1016/j.elecom.2017.01.009>.
- (31) Oezaslan, M.; Liu, W.; Nachtegaal, M.; Frenkel, A. I.; Rutkowski, B.; Werheid, M.; Herrmann, A. K.; Laugier-Bonnaud, C.; Yilmaz, H. C.; Gaponik, N.; et al. Homogeneity and elemental distribution in self-assembled bimetallic Pd-Pt aerogels prepared by a spontaneous one-step gelation process. *Phys Chem Chem Phys* **2016**, *18* (30), 20640-20650. DOI: 10.1039/c6cp03527b.
- (32) Oezaslan, M.; Herrmann, A.-K.; Werheid, M.; Frenkel, A. I.; Nachtegaal, M.; Dosche, C.; Laugier Bonnaud, C.; Yilmaz, H. C.; Kühn, L.; Rhiel, E.; et al. Structural Analysis and Electrochemical Properties of Bimetallic Palladium-Platinum Aerogels Prepared by a Two-Step Gelation Process. *ChemCatChem* **2017**, *9* (5), 798-808. DOI: 10.1002/cctc.201600667.

- (33) Georgi, M.; Klemmed, B.; Benad, A.; Eychmüller, A. A versatile ethanolic approach to metal aerogels (Pt, Pd, Au, Ag, Cu and Co). *Materials Chemistry Frontiers* **2019**, *3* (8), 1586-1592, 10.1039/C9QM00193J. DOI: 10.1039/C9QM00193J.
- (34) Clark, A. H.; Imbao, J.; Frahm, R.; Nachtegaal, M. ProQEXAFS: a highly optimized parallelized rapid processing software for QEXAFS data. *Journal of Synchrotron Radiation* **2020**, *27* (2), 1-7. DOI: doi:10.1107/S1600577519017053.
- (35) Ravel, B.; Newville, M. ATHENA, ARTEMIS, HEPHAESTUS: data analysis for X-ray absorption spectroscopy using IFEFFIT. *Journal of synchrotron radiation* **2005**, *12* (4), 537-541.
- (36) Schmidt, T. J.; Gasteiger, H. A.; Stäb, G.; Urban, P.; Kolb, D.; Behm, R. Characterization of high-surface-area electrocatalysts using a rotating disk electrode configuration. *Journal of The Electrochemical Society* **1998**, *145* (7), 2354-2358.
- (37) Mittermeier, T.; Weiß, A.; Gasteiger, H. A.; Hasché, F. Monometallic Palladium for Oxygen Reduction in PEM Fuel Cells: Particle-Size Effect, Reaction Mechanism, and Voltage Cycling Stability. *Journal of The Electrochemical Society* **2017**, *164* (12), F1081-F1089.
- (38) Gao, D.; Zhou, H.; Wang, J.; Miao, S.; Yang, F.; Wang, G.; Wang, J.; Bao, X. Size-dependent electrocatalytic reduction of CO₂ over Pd nanoparticles. *Journal of the American Chemical Society* **2015**, *137* (13), 4288-4291. DOI: 10.1021/jacs.5b00046.
- (39) Inorganic Crystal Structure Database. Inorganic Crystal Structure Database: See the following: <https://icsd.fiz-karlsruhe.de/> (accessed on June 24, 2021).
- (40) Oezaslan, M.; Strasser, P. Activity of dealloyed PtCo₃ and PtCu₃ nanoparticle electrocatalyst for oxygen reduction reaction in polymer electrolyte membrane fuel cell. *Journal of Power Sources* **2011**, *196* (12), 5240-5249. DOI: <https://doi.org/10.1016/j.jpowsour.2010.11.016>.
- (41) King, H. W.; Manchester, F. D. A low-temperature X-ray diffraction study of Pd and some Pd-H alloys. *Journal of Physics F: Metal Physics* **1978**, *8* (1), 15-26. DOI: 10.1088/0305-4608/8/1/007.
- (42) Swanson, H.; Tatge, E. *Standard X-ray diffraction powder patterns*; 1953.
- (43) Mohsen-Nia, M.; Amiri, H.; Jazi, B. Dielectric constants of water, methanol, ethanol, butanol and acetone: measurement and computational study. *Journal of Solution Chemistry* **2010**, *39* (5), 701-708.
- (44) Van Hyning, D. L.; Zukoski, C. F. Formation mechanisms and aggregation behavior of borohydride reduced silver particles. *Langmuir* **1998**, *14* (24), 7034-7046. Du, R.; Wang, J.; Wang, Y.; Hübner, R.; Fan, X.; Senkovska, I.; Hu, Y.; Kaskel, S.; Eychmüller, A. Unveiling reductant chemistry in fabricating noble metal aerogels for superior oxygen evolution and ethanol oxidation. *Nature Communications* **2020**, *11* (1), 1590. DOI: 10.1038/s41467-020-15391-w.
- (45) Zhang, H.-X.; Wang, C.; Wang, J.-Y.; Zhai, J.-J.; Cai, W.-B. Carbon-Supported Pd-Pt Nanoalloy with Low Pt Content and Superior Catalysis for Formic Acid Electro-oxidation. *The Journal of Physical Chemistry C* **2010**, *114* (14), 6446-6451. DOI: 10.1021/jp100835b.
- (46) Rand, D.; Woods, R. Determination of the surface composition of smooth noble metal alloys by cyclic voltammetry. *Electroanalytical chemistry and interfacial chemistry* **1972**, *36* (1), 57-69.
- (47) Cuesta, A.; Couto, A.; Rincón, A.; Pérez, M. C.; López-Cudero, A.; Gutiérrez, C. Potential dependence of the saturation CO coverage of Pt electrodes: The origin of the pre-peak in CO-stripping voltammograms. Part 3: Pt(poly). *Journal of Electroanalytical Chemistry* **2006**, *586* (2), 184-195. DOI: <https://doi.org/10.1016/j.jelechem.2005.10.006>.
- (48) Jukk, K.; Kongi, N.; Tammeveski, K.; Solla-Gullón, J.; Feliu, J. M. PdPt alloy nanocubes as electrocatalysts for oxygen reduction reaction in acid media. *Electrochemistry*

Communications **2015**, 56, 11-15. Solla-Gullón, J.; Rodes, A.; Montiel, V.; Aldaz, A.; Clavilier, J. Electrochemical characterisation of platinum–palladium nanoparticles prepared in a water-in-oil microemulsion. *Journal of Electroanalytical Chemistry* **2003**, 554, 273-284.

Papageorgopoulos, D. C.; Keijzer, M.; Veldhuis, J. B. J.; de Bruijn, F. A. CO Tolerance of Pd-Rich Platinum Palladium Carbon-Supported Electrocatalysts. *Journal of The Electrochemical Society* **2002**, 149 (11), A1400. DOI: 10.1149/1.1510131.

(49) Álvarez, B.; Climent, V.; Rodes, A.; Feliu, J. M. Anion adsorption on Pd–Pt(111) electrodes in sulphuric acid solution. *Journal of Electroanalytical Chemistry* **2001**, 497 (1), 125-138. DOI: [https://doi.org/10.1016/S0022-0728\(00\)00466-6](https://doi.org/10.1016/S0022-0728(00)00466-6). Álvarez, B.; Berná, A.; Rodes, A.; Feliu, J. M. Electrochemical properties of palladium adlayers on Pt(100) substrates. *Surface Science* **2004**, 573 (1), 32-46. DOI: <https://doi.org/10.1016/j.susc.2004.03.074>.

(50) Hori, Y.; Wakebe, H.; Tsukamoto, T.; Koga, O. Electrocatalytic process of CO selectivity in electrochemical reduction of CO₂ at metal electrodes in aqueous media. *Electrochimica Acta* **1994**, 39 (11), 1833-1839. DOI: [https://doi.org/10.1016/0013-4686\(94\)85172-7](https://doi.org/10.1016/0013-4686(94)85172-7).

(51) Sheng, W.; Myint, M.; Chen, J. G.; Yan, Y. Correlating the hydrogen evolution reaction activity in alkaline electrolytes with the hydrogen binding energy on monometallic surfaces. *Energy & Environmental Science* **2013**, 6 (5), 1509-1512.

(52) Massen, C.; Mortimer-Jones, T. V.; Johnston, R. L. Geometries and segregation properties of platinum–palladium nanoalloy clusters. *Journal of the Chemical Society, Dalton Transactions* **2002**, (23). DOI: 10.1039/b207847c. Lloyd, L. D.; Johnston, R. L.; Salhi, S.; Wilson, N. T. Theoretical investigation of isomer stability in platinum–palladium nanoalloy clusters. *Journal of Materials Chemistry* **2004**, 14 (11), 1691-1704, 10.1039/B313811A. DOI: 10.1039/B313811A. Fernandez, E. M.; Balbas, L. C.; Pérez, L. A.; Michaelian, K.; Garzón, I. L. Structural properties of bimetallic clusters from density functional calculations. *International Journal of Modern Physics B* **2005**, 19 (15n17), 2339-2344. Paz-Borbón, L. O.; Johnston, R. L.; Barcaro, G.; Fortunelli, A. A Mixed Structural Motif in 34-Atom Pd–Pt Clusters. *The Journal of Physical Chemistry C* **2007**, 111 (7), 2936-2941. DOI: 10.1021/jp0674165. Rousset, J.; Bertolini, J.; Miegge, P. Theory of segregation using the equivalent-medium approximation and bond-strength modifications at surfaces: Application to fcc Pd-X alloys. *Physical Review B* **1996**, 53 (8), 4947.

(53) Renouprez, A.; Rousset, J. L.; Cadrot, A. M.; Soldo, Y.; Stieven, L. Structure and catalytic activity of palladium–platinum aggregates obtained by laser vaporisation of bulk alloys. *Journal of alloys and compounds* **2001**, 328 (1-2), 50-56. Fiermans, L.; De Gryse, R.; De Doncker, G.; Jacobs, P. A.; Martens, J. A. Pd Segregation to the Surface of Bimetallic Pt–Pd Particles Supported on H- β Zeolite Evidenced with X-Ray Photoelectron Spectroscopy and Argon Cation Bombardment. *Journal of Catalysis* **2000**, 193 (1), 108-114. DOI: <https://doi.org/10.1006/jcat.2000.2868>. Kolb, U.; Quaiser, S. A.; Winter, M.; Reetz, M. T. Investigation of Tetraalkylammonium Bromide Stabilized Palladium/Platinum Bimetallic Clusters Using Extended X-ray Absorption Fine Structure Spectroscopy. *Chemistry of Materials* **1996**, 8 (8), 1889-1894. DOI: 10.1021/cm960062h. Watson, D. J.; Attard, G. A. Surface segregation and reconstructive behaviour of the (100) and (110) surfaces of platinum–palladium bulk alloy single crystals: a voltammetric and LEED/AES study. *Surface Science* **2002**, 515 (1), 87-93. DOI: [https://doi.org/10.1016/S0039-6028\(02\)01811-3](https://doi.org/10.1016/S0039-6028(02)01811-3).

(54) Ferrando, R.; Jellinek, J.; Johnston, R. L. Nanoalloys: From Theory to Applications of Alloy Clusters and Nanoparticles. *Chemical Reviews* **2008**, 108 (3), 845-910. DOI: 10.1021/cr040090g. Ruban, A. V.; Skriver, H. L.; Nørskov, J. K. Surface segregation energies in transition-metal alloys. *Physical Review B* **1999**, 59 (24), 15990-16000. DOI: 10.1103/PhysRevB.59.15990.

- (55) Zhu, W.; Kattel, S.; Jiao, F.; Chen, J. G. Shape-Controlled CO₂ Electrochemical Reduction on Nanosized Pd Hydride Cubes and Octahedra. *Advanced Energy Materials* **2019**, 9 (9), 1802840. DOI: 10.1002/aenm.201802840 (accessed 2020/03/06). Lee, J. H.; Kattel, S.; Jiang, Z.; Xie, Z.; Yao, S.; Tackett, B. M.; Xu, W.; Marinkovic, N. S.; Chen, J. G. Tuning the activity and selectivity of electroreduction of CO₂ to synthesis gas using bimetallic catalysts. *Nature communications* **2019**, 10 (1), 1-8. Lee, J. H.; Tackett, B. M.; Xie, Z.; Hwang, S.; Chen, J. G. Isotopic effect on electrochemical CO₂ reduction activity and selectivity in H₂O- and D₂O-based electrolytes over palladium. *Chemical Communications* **2020**, 56 (1), 106-108.
- (56) Grdeń, M.; Piaścik, A.; Koczorowski, Z.; Czerwiński, A. Hydrogen electrosorption in Pd–Pt alloys. *Journal of electroanalytical chemistry* **2002**, 532 (1-2), 35-42. Carson, A.; Flanagan, T. B.; Lewis, F. Absorption of hydrogen by palladium/platinum alloys. Part 1.—Electrical resistance as a function of hydrogen content, and one-atmosphere isobars. *Transactions of the Faraday Society* **1960**, 56, 363-370.
- (57) Min, X.; Kanan, M. W. Pd-catalyzed electrohydrogenation of carbon dioxide to formate: high mass activity at low overpotential and identification of the deactivation pathway. *Journal of the American Chemical Society* **2015**, 137 (14), 4701-4708. DOI: 10.1021/ja511890h.
- (58) Herranz, J.; Pătru, A.; Fabbri, E.; Schmidt, T. J. Co-electrolysis of CO₂ and H₂O: From electrode reactions to cell-level development. *Current Opinion in Electrochemistry* **2020**, 23, 89-95. DOI: <https://doi.org/10.1016/j.coelec.2020.05.004>.